

# Interpretation®

## Modeling the interaction between pre-salt seamounts and gravitational failure in salt-bearing passive margins: The Messinian case in the Northwestern Mediterranean Basin

Journal:	<i>Interpretation</i>
Manuscript ID	INT-2016-0096.R2
Manuscript Type:	2016-05 Analog modeling as an aid to structural interpretation
Date Submitted by the Author:	20-Nov-2016
Complete List of Authors:	Ferrer, Oriol; Geomodels Research Institute; University of Barcelona, Department of Earth and Ocean Dynamics Gratacós, Oscar; Geomodels Research Institute; University of Barcelona, Department of Earth and Ocean Dynamics Roca, Eduard; Geomodels Research Institute; University of Barcelona, Department of Earth and Ocean Dynamics Munoz, Josep; Geomodels Research Institute; University of Barcelona, Department of Earth and Ocean Dynamics
Keywords:	modeling, salt, interpretation
Subject Areas:	Structural, stratigraphic, and sedimentologic interpretation, Interpretation concepts, algorithms, methods, and tools

SCHOLARONE™  
Manuscripts

Interpretation

1

1  
2  
3  
4  
5  
6  
7  
8  
9  
10  
11  
12  
13  
14  
15  
16  
17  
18  
19  
20  
21  
22  
23  
24  
25  
26  
27  
28  
29  
30  
31  
32  
33  
34  
35  
36  
37  
38  
39  
40  
41  
42  
43  
44  
45  
46  
47  
48  
49  
50  
51  
52  
53  
54  
55  
56  
57  
58  
59  
60

MODELING THE INTERACTION BETWEEN PRE-SALT SEAMOUNTS AND GRAVITATIONAL FAILURE IN SALT-BEARING PASSIVE MARGINS: THE MESSINIAN CASE IN THE NORTHWESTERN MEDITERRANEAN BASIN

Oriol Ferrer<sup>1</sup>, Oscar Gratacós<sup>1</sup>, Eduard Roca<sup>1</sup> and Josep Anton Muñoz<sup>1</sup>

<sup>1</sup> Geomodels Research Institute. Grup de Geodinàmica i Anàlisi de Conques. Departament de Dinàmica de la Terra i de l'Oceà, Facultat de Ciències de la Terra, Universitat de Barcelona, C/ Martí i Franquès s/n, 08028 Barcelona, Spain

E-mails: [joferrer@ub.edu](mailto:joferrer@ub.edu), [ogratacos@ub.edu](mailto:ogratacos@ub.edu), [eduardroca@ub.edu](mailto:eduardroca@ub.edu), [jamunoz@ub.edu](mailto:jamunoz@ub.edu)

Original paper date of submission: 28<sup>th</sup> June 2016

Revised paper date of submission: 23<sup>rd</sup> October 2016

ABSTRACT

The Northwest Mediterranean Basin includes a thick Messinian salt sequence composed of three evaporitic units. From these the intermediate unit, which is dominantly composed of halite, acts as a gravitational detachment favoring the downslope failure of the overlying sediments in a thin-skinned deformation regime. As a result, the structure of the margin is characterized by an upper extensional domain with basinward-dipping listric normal faults and a lower contractional domain that accommodates upslope extension by folding, salt inflation or diapir squeezing. Lower to middle Miocene volcanic seamounts (pre-salt reliefs) located at the upper extensional domain locally disrupted the evaporitic units and produced salt flow perturbations. They acted as passive buttresses during the gravitational failure modifying the structural zonation of the margin.

## Interpretation

2

Using an experimental approach (sandbox models) this study analyses the role played by seamounts during the kinematic evolution of passive margins and how they alter salt flow and suprasalt deformation during gravitational gliding. The experiments show that seamounts locally interrupt the structural zonation of the margin as they hindered downdip salt flow during early deformation. Seamounts initially compartmentalize the margin architecture, resulting in the development of two gravitational sub-systems with two extensional/contractional pairs that are subsequently re-connected when the accumulation of salt analogue upslope of the relief is enough to overthrust it. From this moment, the cover is passively translated downslope as a regional system. The changes in the viscous layer flow velocity related to the dip differences between the flanks and edges of the seamount determine the kinematic evolution of this system. The experiments also provide geometrical constraints to consider during interpretation of these structures, which are commonly poorly imaged in seismic data.

## INTRODUCTION

The downslope failure of salt-bearing passive margins by gravitational gliding or spreading generates broad zones affected by thin-skinned deformation and produces a well-studied structural zonation (Fig. 1). A typical gravity-driven margin is characterized by wide deformation belts dominated by extensional processes in the upper part linked with a contractional domain in the lower part where the salt pinches-out (e.g., Marton et al., 2000; Brun and Fort, 2004 and 2011; Fort et al., 2004; Hudec and Jackson, 2004 and 2011; Rowan et al., 2004 and 2012, Quirk et al., 2012; Peel, 2014) (Fig. 1). Upslope extension is accommodated by an extensional fault system characterized by basinward-dipping listric faults soling into the salt

## Interpretation

3

1  
2  
3 producing salt rollers and rafts (e.g., Duval et al., 1992; Gaullier et al., 1993; Mauduit et al.,  
4  
5 1997; Mauduit and Brun, 1998; Brun and Maudit, 2009). In contrast, folds, thrusts, and salt  
6  
7 structures (salt-cored anticlines, diapirs or extruding salt sheets) accommodate downslope  
8  
9 contraction (e.g., Fort et al., 2004; Hudec and Jackson, 2004; Rowan et al., 2004. Dooley et al.,  
10  
11 2007). Depending on the margin scale, a third domain may also develop where the overburden is  
12  
13 passively translated basinwards above the salt detachment (Rowan et al., 2004) (Fig. 1).  
14  
15  
16  
17

18  
19 Pre-salt reliefs that act as flow barriers hindering salt drainage can locally disrupt this  
20  
21 classic structural zonation. The reliefs may also act as a nucleation point for secondary  
22  
23 structures. These inherited topographic anomalies may be related to pre-salt folds and faults  
24  
25 (e.g., Adam and Krézsek, 2012) or to a pre-existing topography related to irregularly eroded  
26  
27 surfaces (e.g., Gaullier et al., 1993 and 1996; Maillard et al., 2003) and/or volcanic edifices (e.g.,  
28  
29 Loncke et al., 2006 and 2010; Guennoc et al., 2011; Granado et al., 2016). The continuity of  
30  
31 these reliefs (isolated or linear bodies) and their orientation with respect to the margin slope are  
32  
33 key factors during gravitational failure and suprasalt deformation (Cobbold and Szatmari, 1991;  
34  
35 Gaullier et al., 1993; Gaullier and Bellaiche, 1996; Loncke et al., 2006 and 2010; Augustin et al.,  
36  
37 2014; Feldens and Mitchell, 2015; Dooley and Hudec, this issue; Dooley et al., this issue).  
38  
39  
40  
41  
42  
43

44 All these observations prompt key questions regarding the kinematic evolution of a salt-  
45  
46 bearing passive margin with pre-salt reliefs (specifically seamounts):  
47  
48

- 49 • How does deformation evolve around pre-salt seamounts during gravitational  
50 failure of the margin?  
51
- 52 • What are the main factors intrinsic to the geometry of volcanic edifices that  
53 control the resulting structural style?  
54  
55  
56  
57  
58  
59  
60

Interpretation

4

Using sandbox models and new analysis techniques, this article characterizes salt and suprasalt deformation in response to a pre-salt seamount during gravitational failure of a passive margin. To do so, our experimental programme includes elliptical seamounts with different heights oriented perpendicular to the main salt flow direction. The comparison between experimental results and seismic examples of the North Western Mediterranean Basin depicts that pre-salt seamounts can modify the classical structural zonation of salt-bearing passive margins, hindering salt flow and favoring the development of secondary structures around the relief.

## THE LIGURO-PROVENÇAL BASIN (NORTHWESTERN MEDITERRANEAN)

### *Geological setting*

The Northwestern Mediterranean Basin developed between the Iberian-European continental margin and its Corsica-Sardinia conjugate (Fig. 2). It is an Oligocene-Miocene back-arc basin that formed during the roll-back of the Maghrebian-Tethys oceanic slab below the Iberia-Europe continental lithosphere (Doglioni et al., 1997; Roca et al., 1999; Cavazza et al., 2004; Schettino and Turco, 2010 among others). In this regional setting, the northwestern margin of the basin was affected by a system of NE-trending extensional faults and shear zones that thinned the Iberian-European continental crust to exhume the lower crust/mantle in the abyssal part of the basin (Chamot-Rooke et al., 1997; Bache et al., 2009; Jolivet et al., 2015) (Fig. 2). The formation of this basin was synchronous with late Oligocene-middle Miocene calc-alkaline magmatism that formed volcanic edifices distributed in the intermediate part of the margin as well as in the surrounding areas (Martí et al., 1992; Maillard and Mauffret, 1993; Beccaluva et al., 1994; Roca, 2001; Guennoc et al., 2011).

The study area is located in the central part of the northwestern margin of this basin between the Gulf of Lions and the Liguro-Provençal Basin (Fig. 2). A regional cross-section

## Interpretation

5

1  
2  
3 across this area (Fig. 3) shows the margin architecture with a pre-rift basement that, affected by  
4 latest Eocene (?) to early Miocene (Aquitanian) extensional faults, is overlain by a thick  
5 succession of uppermost Eocene (?) to present-day deposits (Gorini et al., 1993; Roca, 2001;  
6 Jolivet et al., 2015). In this essentially terrigenous succession outlines a major erosive surface  
7 (Margin Erosion Surface or MES in Fig. 3) that basinwards is onlapped by Messinian deposits  
8 (Lofi et al., 2011a and b). This rugged surface exhibiting subaerial erosion features (Stampfli  
9 and Höcker, 1989) is seismically evidenced by an angular unconformity in the upper part of the  
10 margin (Bache et al., 2009). The Messinian deposits include four seismic units ascribed to  
11 different lithological compositions: the Clastic Unit (CU) and the “Messinian evaporitic trilogy”  
12 formed by the Lower Unit (LU), the Mobile Unit (MU) and the Upper Unit (UU) (Lofi et al.,  
13 2011b and Bache et al., 2015).

14  
15  
16  
17  
18  
19  
20  
21  
22  
23  
24  
25  
26  
27  
28  
29 The Lower Unit (LU) is characterized by a set of continuous reflectors with high  
30 amplitude (Lofi et al., 2005 and 2011a; Obone Zue Obame et al., 2011) (Fig. 4). The nature of  
31 this unit is still speculative because it has never been sampled. It has been interpreted as clastic  
32 turbidites (Lofi et al., 2005 and 2011a) that, according to Roveri et al. (2001 and 2008), may  
33 include resedimented gypsum. The LU grades towards the base of the slope to a chaotic and  
34 poorly imaged sedimentary body that, integrated by the Clastic Unit (CU), belongs to alluvial fan  
35 deposits deriving from margin erosion (Gorini et al., 2015; Comeselle and Urgelés, 2016).  
36 Overlying the LU, the intermediate Mobile Unit has transparent seismic facies (Lofi et al., 2005  
37 and 2011a; Obone Zue Obame et al., 2011) (Fig. 4) and has been classically interpreted as  
38 consisting dominantly of halite (Nelly, 1994). Finally, the Upper Unit (UU) corresponds to a  
39 tabular body made up by high amplitude parallel and continuous reflectors (Lofi et al., 2005 and  
40 2011a; Obone Zue Obame et al., 2011) (Fig. 4). It has been correlated to a layered evaporitic  
41  
42  
43  
44  
45  
46  
47  
48  
49  
50  
51  
52  
53  
54  
55  
56  
57  
58  
59  
60

## Interpretation

6

1  
2  
3 sequence and may include dolomitic marls, marls, anhydrites and clastics close to the main  
4  
5  
6 canyons (Lofi *et al.*, 2011a).

7  
8 The deposition of these post-rift Messinian units and the formation of the linked Margin  
9  
10 Erosion Surface (MES) have been related to the huge sea-level drop that took place in the  
11  
12 Mediterranean during the Messinian Salinity Crisis (Hsü *et al.*, 1973). This sea-level drop was  
13  
14 followed by a very fast reflooding in Zanclean (Pliocene) times, which led to the deposition of  
15  
16 clastic deposits in a prograding shelf to a deep-sea fan environment that quickly overlapped both  
17  
18 the Messinian units and the related unconformity (Fig. 3) (Garcia-Castellanos *et al.*, 2009). These  
19  
20 Pliocene to Quaternary deposits derive from the Iberian and European mainland and in the  
21  
22 abyssal plain belong to turbidites deposited in the Rhône and Valencia deep sea fan systems  
23  
24  
25  
26 (Maldonado *et al.*, 1985; Droz *et al.*, 2006).

27  
28  
29 The Messinian dips basinwards (Figs. 3 and 4) as a result of the Plio-Quaternary  
30  
31 differential thermal subsidence between the Northwestern Mediterranean Basin margins and the  
32  
33 basin depocenter (Bessis and Burrus, 1986). This tilting, together with the wedge geometry of  
34  
35 the prograding Plio-Quaternary deposits on the upper margin slope, led to the gravitational  
36  
37 failure of the sediments deposited above the Messinian salt (MU). Thus, the Messinian Upper  
38  
39 Unit (UU) and the Plio-Quaternary deposits were deformed by a combination of gravitational  
40  
41 sliding and spreading processes (Cobbold and Szatmari, 1991; Gaullier, 1993; Gaullier and  
42  
43 Bellaiche, 1996; Dos Reis *et al.*, 2008). The structural style of these materials is characterized by  
44  
45  
46  
47  
48 1) listric normal growth faults dipping basinwards that sole into the upper part of the MU, 2)  
49  
50 contractional detachment folds and squeezed diapirs accommodating upslope extension at the toe  
51  
52 of the margin and 3) a passively translated cover without significant deformation between these  
53  
54  
55  
56  
57  
58  
59  
60

## Interpretation

two domains (Gaullier, 1993; Maillard et al., 2003; Gaullier et al., 2006; Dos Reis *et al.*, 2005 and 2008; Loncke et al., 2006; Obone Zue Obame et al., 2011) (Fig. 4a).

The margin architecture of the Liguro-Provençal Basin is similar to other gravitationally failed passive margins with post-rift salt deposits (e.g the South-Atlantic passive margins of Brazil and Angola) (e.g., Marton et al., 2000; Fort et al., 2004; Hudec and Jackson, 2004; Rowan et al., 2004; Quirk et al., 2012). Furthermore, as seen in these margins, pre-salt seamounts are rather common in the entire Northwestern Mediterranean Basin (Sans and Sàbat, 1993; Guennoc *et al.*, 2011; Granado et al., 2016). They are mainly formed by upper Oligocene - middle Miocene calc-alkaline volcanic edifices (Martí *et al.*, 1992; Beccaluva et al., 1994; Roca, 2001; Maillard et al., 2003). Many of these volcanic edifices remained as islands during the whole Messinian Salinity Crisis episode inducing local changes in salt thickness or even disrupting salt continuity (see Fig. 4 for examples of different levels of salt disruption). Such unhomogeneities had a noticeable influence on the structural evolution of the Liguro-Provençal margins during the gravitational failure (Fig. 4).

## EXPERIMENTAL METHODOLOGY

***Set-up and procedure***

The experimental program presented in this article includes eight analogue models to analyze how the height of a pre-salt seamount modifies the downslope failure of a salt-bearing passive margin (Table 1). Different models with the same setup have been used to examine the temporal evolution of the system (Table 1). According to the case study these seamounts are located between the extensional and contractional domains, where suprasalt deposits are

## Interpretation

8

1  
2  
3 transported basinwards by translation. These models were carried out in a glass-sided  
4 deformation rig that was 110 cm-long, 50 cm-wide and 15 cm-deep (Fig. 5). Seamounts were  
5 built manually with light blue plasticine in order to facilitate the slicing of the models at the end  
6 of the experiment. They were glued to a basal mylar sheet that remained fixed throughout the  
7 experiment. The shape and size of the basal seamount section was the same in all the  
8 experiments, consisting of a rectangle with a semicircle on each short side (Fig. 5a). All of them  
9 had a triangular section in the slope direction with the same height along the rectangular area  
10 (Figs. 5a and 5b). The main difference between the seamounts of the different experiments was  
11 their height, and consequently the average slope angle of their flanks (Table 1).  
12  
13  
14  
15  
16  
17  
18  
19  
20  
21  
22  
23

24 Twelve 2.5 mm-thick layers of alternating white and blue dry sand were deposited above  
25 the basal mylar sheet simulating uppermost Eocene (?) to upper Miocene (Tortonian) clastic  
26 infill of the Liguro-Provençal Basin (Figs. 5b and 5c). Salt equivalent units overlapped the  
27 plasticine seamount. They also pinched out upslope against a 3°-downslope dipping erosional  
28 surface and terminated downslope against a vertical boundary that acted as a frontal buttress  
29 during gravitational failure (Figs. 5a and b).  
30  
31  
32  
33  
34  
35  
36  
37  
38

39 The mechanical stratigraphy of the experimental evaporitic units was designed according  
40 the stratigraphy of the Messinian trilogy in the study area (Fig. 5c). Thus, taking into account  
41 that the LU has been never drilled and may contain resedimented gypsum (Roveri et al., 2001  
42 and 2008) we used a 5 mm-thick layer of a 50% volumetric mixture of sand and a pink  
43 polydimethylsiloxane polymer (Rhodosil GUM FB; Dell'Ertola & Schellart, 2013). This mixture  
44 has a higher effective viscosity than pure polymer (the halite analogue) due to the sandy  
45 impurities (see Callot et al., 2012 and Cartwright et al., 2012). The halite-rich MU, was  
46 simulated using a 10 mm-thick layer of the same polymer but pure and transparent in this case  
47  
48  
49  
50  
51  
52  
53  
54  
55  
56  
57  
58  
59  
60

## Interpretation

(Fig. 5c). Following the methodology proposed by Dooley et al. (2009), different vertical colored polymer plugs located around the plasticine seamount were used as passive markers to trace the flow of the pure polymer during gravitational gliding (Fig. 5a). The mechanical properties of these markers were the same as those of the transparent polymer. Two 2.5 mm-thick layers of white and green silica sand were used as the UU analogue (Fig. 5c). The pre-kinematic package was completed with a 2.5 mm-thick layer of white silica sand covering the entire model and reaching a total thickness of 3 cm (Fig. 5b).

Gravitational gliding was triggered by tilting the baseboard of the rig to 4.5° (Fig. 5b). From that moment, additional syn-kinematic layers of dry white and brown silica sand were added at regular two-hours intervals. Both syn- and pre-kinematic sand was poured into the experimental apparatus and then leveled using a mechanical scraper (Krantz, 1991; Lohrmann et al., 2003). Prior to the deposition of each syn-kinematic sand layer, the baseboard was tilted back to horizontal. This slowed the gravitational flow of the polymer and variations in topography during scanning of the model and deposition of syn-kinematic sand. The regional datum was raised 1.8 mm by each syn-kinematic layer. After the deposition of each syn-kinematic layer the baseboard was tilted again 4.5° in the same direction to re-start the gravitational gliding. At the end, the experiments were covered by post-kinematic sand, preserved and serially sectioned into 3 mm-thick vertical slices.

***Scaling and mechanical properties of the analogue materials***

The fine-grained (199 µm grain size) silica sand used in the experiments deforms according to Navier-Coulomb failure at moderate-high values of normal stress (Horsfield, 1977). The mechanical properties of the poured sand were determined by a shear box test, resulting in

## Interpretation

10

1  
2  
3 an internal friction of  $34.6^\circ$ , a bulk density of  $1500 \text{ kg m}^{-3}$ , a coefficient of internal friction of  
4  
5 0.69 and a low apparent cohesive strength of 55 Pa. In contrast, the pure polymer is a near-  
6  
7 Newtonian viscous fluid with a density of  $972 \text{ kg m}^{-3}$  at room temperature and a viscosity of  $1.6$   
8  
9  $\times 10^{-4} \text{ Pa s}$  when deformed at a laboratory strain rate of  $1.83 \times 10^{-4} \text{ cm s}^{-1}$  (Dell'Ertole and  
10  
11 Schellart, 2013). The 50% by volume mixture of sand and polymer has a density of  $1550 \text{ kg m}^{-3}$   
12  
13 at room temperature and a higher effective viscosity than pure polymer ( $3.35 \times 10^{-4} \text{ Pa s}$ ) when  
14  
15 deformed at the same laboratory strain rate (see Callot et al., 2012 for more information). A  
16  
17 summary of these properties and other experimental scaling parameters are shown in Table 2.  
18  
19  
20  
21  
22  
23

*Analogue models analysis procedure*

24  
25  
26  
27 Model's kinematic was documented and subsequently analyzed by means of oblique and  
28  
29 overhead time-lapse photographs taken every 30 seconds, in combination with model surface  
30  
31 topography recorded before and after the deposition of each syn-kinematic layer using a sub-  
32  
33 millimeter resolution white light scanner (SudioPro from Nub3D).  
34  
35

36  
37 The vertical serial sections carried out at the end of the experiments were also recorded  
38  
39 using high-resolution digital cameras to analyze the variation in the structures along strike. A 4-  
40  
41 cm wide section along each side of the experiments was omitted in the analysis to avoid border  
42  
43 effects related to the friction between glass sidewalls and the sandpack. High-resolution  
44  
45 photographs of the model cross sections were used to reconstruct a 3D voxel model in image-  
46  
47 processing software allowing the generation of virtual strike and depth slices (see Dooley et al.,  
48  
49 2009 for further details).  
50  
51  
52  
53  
54  
55  
56  
57  
58  
59  
60

## EXPERIMENTAL RESULTS

***Baseline model (without seamount)***

We performed a baseline experiment without a seamount (Table 1) to illustrate the main structural features resulting from the tilting of the modeled passive margin. The experimental results illustrate a structural zonation similar to other salt-bearing passive margins, characterized by upslope extension, downslope contraction and an intermediate translational domain (e.g., Marton et al., 2000; Brun and Fort, 2004 and 2011; Fort et al., 2004; Hudec and Jackson, 2004 and 2011; Rowan et al., 2004 and 2012; Quirk et al., 2012; Peel, 2014) (Fig. 6a). As occurs in natural cases, deformation of the sand layers (sedimentary overburden) during tilting is driven by gravitational failure above the pure polymer (regional detachment) as it flows downslope. As a result, the thickness of the polymer decreases upslope in the extensional domain and increases downslope in the contractional domain (Fig. 6a). In contrast, the more viscous LU modeled by the sand and polymer mixture maintained a constant thickness throughout the experiment (Fig. 6a).

A set of basinward dipping listric normal growth faults rooted in the transparent polymer developed in the upslope extensional domain (Duval et al., 1992; Gaullier et al., 1993; Mauduit et al., 1997; Mauduit and Brun, 1998; Brun and Fort, 2004 and 2011; Brun and Mauduit, 2009; Carthwright et al., 2012) (Fig. 6a). While different rollovers grew in the hanging walls of these listric faults, polymer trapped in the footwalls as salt rollers (Duval et al., 1992; Gaullier, 1993; Mauduit and Brun, 1998; Brun and Mauduit, 2009). The strike of these faults was parallel to the upslope polymer pinch-out that constrains the location of the peripheral faults (Fig. 6a). Extensional faults propagated basinward becoming younger downslope. Upslope regional

## Interpretation

12

1  
2  
3 extension was accommodated by downslope contraction developing incipient detachment folds  
4  
5 at the beginning of gravitational gliding. The growth of these folds was usually aborted by syn-  
6  
7 kinematic sedimentation that strengthens their roofs by thickening during early gravitational  
8  
9 gliding. After 3 hours, the outermost fold belt evolved to a simple thrust verging basinwards  
10  
11 above the downslope edge of the polymer layer that experience inflation by buttressing (Fig. 6a).  
12  
13 In contrast, the overburden of the intermediate translational domain was passively transported  
14  
15 downslope above the transparent polymer with no obvious visible deformation (Fig. 6a).  
16  
17  
18  
19  
20  
21  
22  
23  
24

***Models with seamounts***

25  
26  
27  
28 The structural style of the upslope extensional and downslope contractional domains of  
29  
30 models with seamounts is very similar to the baseline model (comparison of Figs. 6a and 6c).  
31  
32 Whereas different listric normal faults dipping basinwards formed upslope after 6 hours of  
33  
34 gravitational gliding, a detached fold belt evolving into a simple thrust developed downslope <sup>at</sup> ~~in~~  
35  
36 the salt pinch-out (Fig. 6c). If gravitational gliding continues (e.g., models with 18 hours of  
37  
38 gravitational gliding, Fig. 6b), the extensional domain widens, with younger faults progressively  
39  
40 developing downslope. The increase of extensional deformation is balanced downslope by a  
41  
42 second thrust developed in a break-back sequence and by polymer inflation (Fig. 6b).  
43  
44  
45  
46  
47

48  
49 However, the main difference between models with and without a seamount is the  
50  
51 interruption of polymer flow by pre-salt reliefs. The kinematic evolution of the overburden in  
52  
53 models with a seamount clearly depends on the position of their summit lying below or above the  
54  
55 top salt at the beginning of the experiment. Thus, the seamount partially blocks salt flow when  
56  
57  
58  
59  
60

## Interpretation

13

1  
2  
3 their summit lies below the top salt (Fig. 6b). In contrast, the salt flow is totally blocked when  
4  
5 the summit lies above the top salt (Fig. 6c). This entails the development of secondary structures  
6  
7 around the seamount that in the second case disrupts the continuity of the translational domain  
8  
9 (Fig. 6c). The following sections of the manuscript introduce the main structural elements as well  
10  
11 as the kinematic evolution of both cases.  
12  
13  
14  
15  
16  
17  
18  
19

20 *Seamount does not fully block salt flow – summit lies below top salt*  
21  
22

23  
24 In the case whereby the seamount lies below top salt cover deformation is characterized by a  
25  
26 regional extensional-contractional system that continually glides basinwards throughout the  
27  
28 experiment (Fig. 6b). At the beginning of the gravitational failure, the seamount partially  
29  
30 opposed to polymer flow and hampered its drainage. Buttressing favored polymer inflation  
31  
32 upslope of the seamount slightly raising the top of the initial regional datum (Fig. 7a). Coeval  
33  
34 with polymer inflation, the development of a syncline downslope of the seamount occurred in  
35  
36 conjunction with the consequent thinning of the pure polymer layer (Fig. 7a). An incipient  
37  
38 collapse graben may develop during the early deformation at the crest of the anticline (Fig. 7b).  
39  
40 Syn-kinematic layers overlapped the pre-kinematic unit above the syncline and progressively  
41  
42 offlapped upslope of the seamount due to polymer inflation (Fig. 7a).  
43  
44  
45  
46  
47

48  
49 As the model evolved downdip polymer flow fed the anticline that was gradually translated  
50  
51 downdip (Fig. 7b). The interaction between the syn-kinematic sedimentation and the anticline  
52  
53 growth produced an erosive unconformity that climbed through younger syn-kinematic units.  
54  
55 Basinwards this unconformity evolved into a paracomformity (Fig. 7b). Taking into account that  
56  
57  
58  
59  
60

## Interpretation

14

1  
2  
3 the seamount is fixed during the experiments, the upslope migration of syn-kinematic  
4 depocenters and onlaps (Fig. 7) indicates that the basin depocenter maintain a relatively fixed  
5 position during gravitational gliding. Thus, for the last stages of deformation, the syn-kinematic  
6 sand layers filling the syncline were deposited above uplifted areas previously located upslope of  
7 the seamount. This is noticed because older syn-kinematic layers were absent or pinched-out  
8 downslope against the unconformity (Fig. 7b).  
9  
10  
11  
12  
13  
14  
15  
16

17  
18  
19  
20  
21  
22 *Seamount fully blocks salt flow – summit lies above top salt*  
23

24  
25  
26 In this situation, the height of the seamount lying above top salt plays a key role in the regional  
27 structural style and the kinematic evolution of the model. In order to understand how is the  
28 temporal evolution when seamounts fully blocks salt flow, we used different models with the  
29 same initial setup but with different lengths (Table 1 and Fig. 8). The variation in the ratio  
30 between seamount height and top salt throughout the experiment highlights two distinct  
31 evolutionary stages.  
32  
33  
34  
35  
36  
37  
38  
39

40  
41 During the first stage, the seamount locally interrupts the lateral continuity of the pure polymer  
42 layer and compartmentalizes the three-domain gravitational system into two extensional-  
43 contractional sub-systems (Figs. 6c, 8a and 9b to d). Updip extension was accommodated  
44 upslope of the seamount by polymer thickening and the development of a downdip-verging  
45 thrust (structure 1 in Fig. 8a). A “hanging-wall terrace” formed by the UU was preserved in the  
46 footwall of this thrust attached to the seamount. Thrust propagation uplifted the regional  
47 controlling the offlap terminations of the syn-kinematic layers in the backlimb of the hanging  
48  
49  
50  
51  
52  
53  
54  
55  
56  
57  
58  
59  
60

## Interpretation

1  
2  
3 wall anticline (Fig. 8a). In contrast, a major listric normal fault rooted in the pure polymer flank  
4  
5 (structure 2 in Fig. 8a) controlled the development of the basin. Thin-skinned extension triggered  
6  
7 the rise of reactive ridges along the extensional faults of the basin (Vendeville and Jackson,  
8  
9 1992; Hudec and Jackson, 2011) (Figs. 8a, 9b to 9d and 10b). These ridges converged towards  
10  
11 the central part of the basin leading to an active diapir (Fig. 9c). At the last stages of this first  
12  
13 episode the pure polymer layer was continuous below the basin, being practically depleted below  
14  
15 the hanging wall of the main extensional fault (structure 2 in Fig. 8a). This prevented the  
16  
17 downdip flow of the pink layer (sand-polymer mixture). The forelimb of the hanging wall  
18  
19 anticline above the seamount collapsed when the overburden reached the summit of the  
20  
21 seamount at the end of this first stage. As a consequence debrites deposits were incorporated to  
22  
23 the third syn-kinematic layer of the basin (greenish sand on Fig. 8a).  
24  
25  
26  
27  
28  
29

30 The second stage begins when top salt ride above the seamount and it was overthrust by the  
31  
32 upslope cover using the pure polymer as a detachment (Figs. 8b, 8c and 9e to 9h). At this point,  
33  
34 the kinematics of the model dramatically changes and the two gravitational sub-systems are re-  
35  
36 connected. The time sequence evolution of figures 8b and 8c shows how after re-connection the  
37  
38 entire margin is translated downslope as a unique extensional-contractional system. As the model  
39  
40 evolved, the structure around the seamount becomes much more complex with progressive  
41  
42 overlap of the contractional and extensional zones downslope of the relief (Fig. 8b and 8c).  
43  
44 Downslope of the seamount, the structural style dramatically changed after polymer depletion  
45  
46 (Figs. 8b, 10b and 10f). This is the beginning of a gradual attenuation of the pre-existing  
47  
48 structures (Fig. 9d to 9h). After welding, the basin was passively transported downslope above  
49  
50 the main normal fault that initially developed attached to the downslope flank of the seamount  
51  
52 (structure 2 in Fig. 8). Although the pink layer has a higher effective viscosity than pure  
53  
54  
55  
56  
57  
58  
59  
60

Interpretation

16

1  
2  
3 polymer, the total depletion of the pure polymer triggered the flow of the sand-polymer mixture  
4  
5 that acted as a less efficient detachment (Figs. 8b, 8c, 10f and 10g).  
6  
7

8  
9 The combined effect of cover overthrusting and welding also forced the development of a  
10  
11 gravitationally linked contractional zone downslope of the seamount (Figs. 8b, 10b and 11). The  
12  
13 structural style of this contractional zone results from the interaction between the height  
14  
15 difference between the crest of the anticline above the seamount and the basin as well as from  
16  
17 the syn-kinematic sedimentation rate. The most important height difference occurred during the  
18  
19 early overthrusting and was coeval to the development of the first thrust and the maximum  
20  
21 development of debrites (layers 3 and 4 of Fig. 11). The gradual height attenuation between the  
22  
23 crest of the anticline and the adjacent basin during overthrusting resulted in a progressive  
24  
25 reduction of the debrites volume (layers 5 and 6 of Fig. 11). The syn-kinematic sedimentation  
26  
27 rate applied to our models aborted the growth of these folds and thrusts. A prominent angular  
28  
29 unconformity developed as a result of the interaction between the growth of the gravitational  
30  
31 linked contractional structures and the sedimentation rate (dashed lines in Figs. 8 and 11). The  
32  
33 syn-kinematic layers of the basin onlapped against the partly eroded overthrust syn-kinematic  
34  
35 layers and the offlaps developed upslope of the seamount (Fig. 11).  
36  
37  
38  
39  
40  
41  
42  
43  
44  
45

## 46 DISCUSSION

47  
48  
49 **What is the impact of a pre-salt seamount on the regional structure of a salt-bearing**  
50  
51 **passive margin?**  
52  
53  
54  
55  
56  
57  
58  
59  
60

## Interpretation

17

1  
2  
3 The presence of linear pre-salt seamounts in a salt-bearing passive margin can modify the  
4 regional structure because seamounts interrupt the continuity of the evaporitic unit. Depending  
5 on the height differences between the seamount summit and the top of the viscous layer, this  
6 disruption can lead to significant changes in the classical structural zonation of such margins.  
7  
8 Seamounts initially hinder salt drainage during early gravitational failure by acting as a passive  
9 buttress to flow. Our physical models show that when the summit of the seamount lies below top  
10 salt (experiments 1 and 1a, Table 1), the cover glides downslope as a unique extensional-  
11 contractional system encompassing an intermediate translational zone. The syn-kinematic units  
12 of the translational domain show significant thickness variations related to the development of a  
13 basin downslope of the seamount (Figs. 6b and 7). In contrast, two well-differentiated  
14 gravitational sub-systems with upslope extension and downslope contraction develop when the  
15 summit of the seamount is located near or above the top of the polymer layer (experiments 2 to  
16 5, Table 1) (Fig. 6c). Here, the structural style of both pairs is slightly different. Although listric  
17 faults develop in the extensional domain of both sub-systems, these differ on number, spacing  
18 and slip (Fig. 6c). These differences are basically induced by the thickness of the pure polymer  
19 prior to the gravitational deformation (Fig. 6c) and the slope angle of the seamount flank (Figs. 8  
20 and 12b, Table 1). Similarly, the dip of the thrusts developed upslope of the seamount is steeper  
21 than the thrusts related to the pure polymer downslope pinch-out (Fig. 6c). Here the main control  
22 factor is the relative height of the seamount summit above the top of the pure polymer at the  
23 beginning of the gravitational gliding. Both contractional sub-systems are extremely different for  
24 model 6 (Table 1, Fig. 12) in which the distance between the summit of the seamount and the top  
25 of the polymer does not allow cover overthrusting. As a result, buttressing produced by the  
26  
27  
28  
29  
30  
31  
32  
33  
34  
35  
36  
37  
38  
39  
40  
41  
42  
43  
44  
45  
46  
47  
48  
49  
50  
51  
52  
53  
54  
55  
56  
57  
58  
59  
60

Interpretation

18

upslope seamount flank enhanced the development of a backthrust with an associated piggy-back basin (Fig. 12).

### **How do seamounts affect the salt flow pattern during gravitational failure of the margin?**

The experimental programme presented in this article depicts how a pre-salt relief hinders drainage of a viscous polymer induced by tilting. A contour map of the top of the pure polymer illustrates the zones where polymer was depleted or accumulated during gravitational gliding (Fig. 13a). It clearly shows how the polymer thickened upslope of the seamount before being able to flow over the summit and carries the roof with it as an overthrust (white blue colors above the black dashed line). This map also shows how a passive diapir developed downslope of the seamount (Fig. 13a). This diapir is surrounded by four welded basins separated by arcuate polymer ridges. The colored polymer plugs introduced in the pure polymer around the seamounts (Fig. 5a) allowed us to track the effect of the seamounts on polymer flow during gravitational gliding (Fig. 13). Depending on their location, these cylindrical markers were deformed in different ways. The outermost, located symmetrically at both ends of the seamount (blue and red markers with numbers 1, 5, 6 and 10 in Fig. 13b or blue polymer in Fig. 10a), were essentially deformed following straight trajectories parallel or slightly oblique to the regional dip direction. The top of these markers is the most seaward part of them, depicting a strong component of Couette flow related to the shearing of the pure polymer by downslope translation of the overburden (Fig. 10a).

In contrast, the polymer plugs around the seamount reveal a complex streamlines patterns and related flow velocities as suggested by areas of plug inflation and deflation (Fig. 13b). The deformation of the central blue marker located updip of the seamount is controlled by the

## Interpretation

1  
2  
3 seamount height and the initial thickness of pure polymer. So, when the seamount summit lies  
4 above the top polymer (e.g., experiment 6, Fig. 12) the polymer cannot flow over it and the  
5  
6 central marker deforms with a divergent flow pattern. Two horns with opposite streamline  
7  
8 directions developed parallel to the seamount trend. These morphological variations imply  
9  
10 significant variations in flow velocity that progressively decrease until the polymer reaches the  
11  
12 summit of the seamount. An increase in flow velocity took place during overthrusting as a  
13  
14 consequence of the progressive polymer thickening above the seamount. The yellow markers  
15  
16 located upslope of the seamount (numbers 2 and 4 in Fig. 13b), show how the streamlines avoid  
17  
18 the seamount using a curved trajectory or bypass. This divergent pattern considerably reduces the  
19  
20 distance between streamlines, indicating an increase in flow velocity. Streamlines show a  
21  
22 convergent pattern once the yellow markers surpass the seamount (Fig. 13). This is probably  
23  
24 constrained by the development of the basin downslope of the seamount (Fig. 13b). On a  
25  
26 different way, the sinking of the basin and the gravitational gliding stretched the three markers  
27  
28 downslope of the seamount (numbers 6, 7 and 8 in Fig. 13). At the beginning of gravitational  
29  
30 gliding they show a marked Couette flow component (e.g., red marker on Fig. 7b). As  
31  
32 gravitational gliding progressed, the polymer initially below the basin was expelled down dip.  
33  
34 The pressurized polymer moved towards the passive diapir – pressure release – showing a  
35  
36 convergent streamlines trajectory. Figure 13b shows how the red markers followed the ridges  
37  
38 between the welded areas to feed the central passive diapir. In the cross-section of figure 13c  
39  
40 these red markers show a plume shape that reaches the surface of the diapir. The development of  
41  
42 this plume was forced by the inward injection of the transparent polymer during the rise of the  
43  
44 passive diapir (Dooley et al., 2009). Downslope of the diapir, the red markers show a divergent  
45  
46 flow pattern following the ridges between the welded areas (Fig. 13b).  
47  
48  
49  
50  
51  
52  
53  
54  
55  
56  
57  
58  
59  
60

## COMPARISON WITH THE LIGURO-PROVENÇAL BASIN

The gravitational system documented in our baseline model (Fig. 6a) is broadly similar to the geometries of the study area when seamounts are absent or their summit do not reaches the Messinian salt (Fig. 4a). In both cases, the salt unit is continuous and flows downdip. A set of listric normal faults dipping basinwards developed in the upper part of the margin (Gaullier, 1993; Gaullier et al., 1993; Reis et al., 2008) (Fig. 4a). Upslope extension is accommodated downslope by detachment folds and squeezed diapirs (Gaullier, 1993; Gaullier and Bellaiche, 1996; Reis et al., 2005 and 2008) (Fig. 4a). In between the practically undeformed overburden is gravitationally translated using the MU as a detachment (Gaullier, 1993; Reis et al., 2008) (Fig. 4a). Although the structural style of the extensional system is similar (Figs. 10b and 13a), the contractional system differs greatly between nature and the experiments (compare Figs. 4a and 6a). While detachment folds and squeezed diapirs are common in the Liguro-Provençal Basin (Fig. 4a), buckle folds were quickly aborted in our physical models evolving into different thrusts emplaced in a break-back sequence (Fig. 6b). The early detachment folds were buried due to the high sedimentation rate applied to our models developing a thick and strong overburden that inhibited folding. In contrast, thrust development is basically constrained by the downslope vertical edge of the salt basin, which acts as a nucleation point for the first thrust. However, in the Liguro-Provençal Basin, there is no downdip salt pinch-out, except towards the Balearic Islands and Corsica (Lofi et al., 2011a). Elsewhere, the salt layer is continuous from Marseille to Algiers (e.g., Gaullier and Bellaiche, 1996; Dos Reis et al., 2005; Lofi et al., 2011a).

## Interpretation

21

1  
2  
3 Our physical models predict that the presence of seamounts in the translational domain of  
4 the Liguro-Provençal Basin could significantly impact the margin architecture (Figs. 4b and 4c).  
5  
6 The effect of seamounts on the margin deformation occurs at two different scales. At a regional  
7  
8 scale, they could interrupt the continuity of the translational domain, resulting in the  
9  
10 development of two gravitational sub-systems (Figs. 4b and 4c). In addition, they locally control  
11  
12 the development of contractional and extensional structures upslope and downslope of the  
13  
14 seamount respectively (Figs. 4b and c). The structural style of the upslope structures clearly  
15  
16 differs between experiments and seismic data. Salt inflated areas (Fig. 4b) or asymmetric buckle  
17  
18 folds (Fig. 4c) have been interpreted upslope seamounts in seismic profiles. In our experiments  
19  
20 polymer inflates until it can flow over the seamount (Figs. 8a and 8b). Downdip-verging thrusts  
21  
22 form in the overburden as the roof is carried over the pre-salt high. On the other hand, a  
23  
24 backthrust develops when the salt inflated area upslope the seamount cannot reach the summit of  
25  
26 the relief (experiment 6, Table 1, Fig. 12). Despite this, no thrust has been interpreted upslope of  
27  
28 the seamounts in the studied dataset. Taking into account the limitations of 2D seismic for the  
29  
30 characterization of complex tridimensional structures, the lack of thrusts may be related to  
31  
32 several factors: 1) the amount of shortening (less than in our experiments); 2) the shape of the  
33  
34 seamount (the buttressing for isolated circular seamounts may be small or non-existent); 3) the  
35  
36 volume of salt available upslope of the seamounts; 4) the composition of the halite of the MU  
37  
38 that could become less pure at the basin margin; or 5) the deformation rate of evaporites (slower  
39  
40 for the Liguro-Provençal Basin due to progressive tilting but constant throughout our  
41  
42 experiments).  
43  
44  
45  
46  
47  
48  
49  
50  
51  
52  
53  
54  
55  
56  
57  
58  
59  
60

## Interpretation

22

1  
2  
3  
4  
5  
6  
7  
8  
9  
10  
11  
12  
13  
14  
15  
16  
17  
18  
19  
20  
21  
22  
23  
24  
25  
26  
27  
28  
29  
30  
31  
32

Additionally, the LU has been never sampled in the Liguro-Provençal Basin and its composition is speculative (clastic turbidites and resedimented gypsum, according to Roveri et al. 2001 and 2008). The approximation we have used as analogue of this unit is a material with a higher effective viscosity than pure polymer based on a mixture of sand and polymer (Callot et al., 2012). However, the experiments with a greater gravitational gliding clearly show that after pure polymer depletion, the weight of the basin triggered the deformation of this material (Figs. 8b and 8c). The seismic profiles studied in this project clearly show that the LU remains undeformed in the Liguro-Provençal Basin. This could be related to the mechanical properties of this unit, which are likely closer to a brittle behavior.

## CONCLUSIONS

33  
34  
35  
36  
37  
38  
39  
40  
41  
42

The presence of pre-salt relief in the form of a seamount can modify the three domain structural zonation of salt-bearing passive margins developing two gravitational sub-systems separated by the seamount. These are characterized by upslope extension and downslope contraction

43  
44  
45  
46  
47  
48  
49  
50  
51  
52  
53  
54  
55  
56  
57  
58  
59  
60

The structural style and kinematics of both margin-wide and local structures may change during gravitational gliding if the amount of salt upslope of the seamount is sufficient to overtake the relief. Thus, depending on the seamount height with respect the top of the evaporitic unit, seamounts can act as temporary barriers during margin evolution, resulting in two different stages. During the first stage, the seamount initially hinders salt flow, forcing salt migration around the relief. As a consequence of the buttress upslope of the seamount, a thrust develops

## Interpretation

23

1  
2  
3 and gradually uplifts the cover. When the cover reaches the height of the relief, the seamount is  
4  
5 overthrust, and falls rapidly downslope along the seamount flank. A significant increase in salt  
6  
7 flow velocity occurs coeval with overthrusting. The development of a primary weld below the  
8  
9 basin downslope of the seamount and the flow velocity decrease that occurs at the edge of the  
10  
11 seamount favors the formation of an fold and thrust system.  
12  
13  
14  
15

16 The seamounts hinder salt flow, forcing the development of a divergent pattern in the  
17  
18 polymer streamlines surrounding the relief during gravitational gliding. Streamlines deviation  
19  
20 also occur where there are diapirs allowing salt to escape vertically from beneath the basins. In  
21  
22 contrast, streamlines in areas without seamounts or diapirs describe dominantly linear traces  
23  
24 parallel to the dip direction of the passive margin.  
25  
26  
27  
28

29 The experimental results included in this manuscript provide a set of geometrical  
30  
31 constraints that can be used in seismic interpretation of similar structures in margins with pre-salt  
32  
33 seamounts (e.g., Eastern Mediterranean, Red Sea, offshore Morocco). Because the seismic  
34  
35 dataset available for the study area is 2D, analogue models also allow us to infer the three-  
36  
37 dimensional geometry of the supra-salt structures.  
38  
39  
40  
41  
42  
43  
44  
45  
46  
47  
48

## ACKNOWLEDGMENTS

49  
50  
51  
52  
53 OF dedicates this article to the memory of M.P.A. Jackson who guided my first steps in  
54  
55 salt tectonics. We gratefully acknowledge V. Gaullier, B.C. Vendeville and T. Dooley for their  
56  
57  
58  
59  
60

Interpretation

24

1  
2  
3 helpful comments and reviews. This research was funded by the SALTECRES project  
4  
5 (CGL2014-54118-C2-1-R MINECO/FEDER, UE) as well as the *Grup de Recerca de*  
6  
7 *Geodinàmica i Anàlisi de Conques* (2014SRG467). The Geomodels Analogue Modeling  
8  
9 Laboratory was supported by a Scientific Infrastructure (UNBA08-4E-006) co-funded by the  
10  
11 European Regional Development Fund of the *Ministerio de Ciencia e Innovación* of the Spanish  
12  
13 Government and Statoil. *Paradigm<sup>TM</sup>*, *Midland Valley* and *IHS* are also acknowledged for  
14  
15 providing *Gocad*, *Move* and *Kingdom Suite* softwares.  
16  
17  
18  
19

## REFERENCES

20  
21  
22  
23  
24 Adam, J., and C. Krézsek, C., 2012, Basin-scale salt tectonic processes of the Laurentian  
25  
26 Basin, Eastern Canada: insights from integrated regional 2D seismic interpretation and 4D  
27  
28 physical experiments, *in* G.I. Alsop, S.G. Archer, A.J. Hartley, N.T. Grant, and R. Hodgkinson,  
29  
30 eds., *Salt Tectonics, Sediments and Prospectivity*: Geological Society, London Special  
31  
32 Publications, 363, 331-360.  
33  
34  
35  
36

37  
38 Augustin, N., C. W. Devey, F.M. Van der Zwan, P. Feldens, M. Tominaga, R.A. Bantan,  
39  
40 and T. Kwasnitschka, 2014, The rifting to streading transition in the Red Sea: Earth and  
41  
42 Planetary Science Letters, **395**, 217-230.  
43  
44  
45

46  
47 Bache, F., J.-P. Olivet, M. Rabineau, J. Baztan, D. Aslanian and J.-P. Suc, 2009,  
48  
49 Messinian erosional and salinity crises: View from the Provence Basin (Gulf of Lions, Western  
50  
51 Mediterranean): Earth and Planetary Science Letters, **286**, 1-2, 139-157.  
52  
53

54  
55 Bache, F., J. Gargani, J.-P. Suc, C. Gorini, M. Rabineau, S.-M. Popescu, E. Leroux, D.  
56  
57 Do Couto, G. Jouannic, J.-L. Rubino, J.-L. Olivet, G. Clauzon, A.T. Dos Reis and D. Aslanian,  
58  
59  
60

## Interpretation

2015, Messinian evaporite depositon during sea level rise in the Gulf of Lions (Western Mediterranean): *Marine and Petroleum Geology*, **66**, 262-277.

Beccaluva, L., M. Coltorti, R. Galassi, G. Macciotta and F. Siena, 1994, The Cainozoic calcalkaline magmatism of the western Mediterranean and its geodynamic significance: *Bolletino di Geofisica Teorica ed Applicata*, **36**, 293-309.

Bessis, F., and J. Burrus, 1986, Étude de la subsidence de la marge du Golfe du Lion (Méditerranée Occidentale): *Bulletin des Centres de Recherche et Exploration-Production Elf-Aquitaine*, **10**, 123-141.

Brun, J.-P., and X. Fort, 2004, Compressional salt tectonics (Angolan margin): *Tectonophysics*, **382**, 129-150.

Brun, J.-P., and X. Fort, 2011, Salt tectonics at passive margins: Geology versus models: *Marine and Petroleum Geology*, **28**, 1123-1145.

Brun, J.-P., and T.P.O. Mauduit, 2009, Salt rollers: structure and kinematics from analogue modelling: *Marine and Petroleum Geology*, **26**, 249-258.

Callot, J.-P., V. Trocmé, J. Letouzey, E. Albouy, S. Jahani, S. Sherkati, 2012, Pre-existing salt structures and the folding of the Zagros Mountains, *in* G.I. Alsop, S.G. Archer, A.J. Hartley, N.T. Grant, and R. Hodgkinson, eds., *Salt Tectonics, Sediments and Prospectivity: Geological Society, London Special Publications*, **363**, 545-561.

Cameselle, A.L., and R. Urgelés, 2016, Large-scale margin collapse during Messinian early sea-level drawdown: the SW Valencia trough, NW Mediterranean: *Basin Research* doi:10.1111/bre.12170

## Interpretation

26

1  
2  
3 Cartwright, J., M.P. Jackson, T. Dooley, and S. Higgins, 2012, Strain partitioning in  
4 gravity-driven shortening of a thick, multilayered evaporite sequence, *in* G.I. Alsop, S.G. Archer,  
5 A.J. Hartley, N.T. Grant, and R. Hodgkinson, eds., *Salt Tectonics, Sediments and Prospectivity*:  
6 Geological Society, London Special Publications, **363**, 449-470.  
7  
8  
9  
10  
11

12  
13  
14 Cavazza, W., F. Roure, W. Spakman, G.M. Stampfli, and P.A. Ziegler, 2004, The  
15 TRANSMED Atlas – The Mediterranean Region from Crust to Mantle: Springer, Berlin-  
16 Heidelberg.  
17  
18  
19  
20  
21

22 Chamot-Rooke, N., F. Jestin, and J.M. Gaulier, 1997, Constraints on the Moho depth and  
23 crustal thickness in the Liguro-Provençal Basin from 3D gravity inversion: Geodynamic  
24 implications: *Revue de l'Institut Français du Pétrole*, **52**, 557-583.  
25  
26  
27  
28  
29

30 Cobbold, P.R. and P. Szatmari, 1991, Radial gravitational gliding on passive margins:  
31 *Tectonophysics*, **188**, 249–289.  
32  
33  
34  
35

36 Dell'Ertale, D., and W.P. Schellart, 2013, The development of sheath folds in viscously  
37 stratified materials in simple shear conditions: an analogue approach: *Journal of Structural*  
38 *Geology*, **56**, 129-141.  
39  
40  
41  
42  
43

44 Doglioni, C., E. Gueguen, F. Sàbat, and M. Fernández, 1997, The Western Mediterranean  
45 extensional basins and the Alpine Orogen: *Terra Nova*, **9**, 109-112.  
46  
47  
48  
49

50 Dooley, T.P., M.P.A. Jackson, and M.R. Hudec, 2007, Initiation and growth of salt-based  
51 thrust belts on passive margins: results from physical models: *Basin Research*, **19**, 165-177.  
52  
53  
54  
55  
56  
57  
58  
59  
60

## Interpretation

27

1  
2  
3 Dooley, T.P., M.P.A. Jackson, and M.R. Hudec, 2009, Inflation and deflation of deeply  
4 buried salt stocks during lateral shortening: *Journal of Structural Geology*, **31**, 582-600.  
5  
6

7  
8  
9 Dooley, T.P., M.R. Hudec, D. Garruthers, M.P.A. Jackson and G. Luo (in this issue), The  
10 effects of base-salt relief on salt flow and suprasalt deformation patterns – Part 1: Flow across  
11 simple steps in the base of salt: *Interpretation*,  
12  
13  
14

15  
16  
17 Dooley, T.P. and M.R. Hudec (in this issue), The effects of base-salt relief on salt flow  
18 and suprasalt deformation patterns – Part 2: Application to the Eastern Gulf of Mexico:  
19  
20  
21  
22 *Interpretation*,  
23  
24

25  
26 Dos Reis, A.T., C. Gorini, and A. Mauffret, 2005, Implications of salt-sediment  
27 interactions for the architecture of the Gulf of Lions deep-water sedimentary systems – Western  
28 Mediterranean: *Marine and Petroleum Geology*, **22**, 713-746.  
29  
30  
31

32  
33  
34 Dos Reis, A.T., C. Gorini, W. Weibull, R. Perovano, M. Mepen, and É. Ferreira, 2008,  
35 Radial gravitational gliding indicated by subsalt relief and salt-related structures: the example of  
36 the Gulf of Lions, Western Mediterranean: *Revista Brasileira de Geofísica*, **26**, 347-365.  
37  
38  
39

40  
41  
42 Droz, L., A.T. Dos Reis, M. Rabineau, S. Berné, and G. Bellaiche, 2006, Quaternary  
43 turbidite systems on the northern margins of the Balearic Basin (Western Mediterranean): A  
44 synthesis: *Geo-Marine Letters*, **26**, 347-359.  
45  
46  
47  
48

49  
50  
51 Duval, B., Cramez, C., and M.P.A. Jackson, 1992, Raft tectonics in the Kwanza Basin,  
52 Angola: *Marine and Petroleum Geology*, **9**, 389-404.  
53  
54  
55  
56  
57  
58  
59  
60

## Interpretation

28

1  
2  
3  
4  
5  
6  
7  
8  
9  
Feldens, P., and N.C. Mitchell, 2015, Salt flows in the Central Red Sea, *in* N.M.A. Rasul, and I.C.F. Stewart, eds., *The Red Sea: Springer Earth System Sciences*. Berlin Heidelberg, Springer, 205-218.

10  
11  
12  
13  
14  
Fort, X., J.-P. Brun, and F. Chauvel, 2004, Salt tectonics on the Angolan margin, synsedimentary deformation processes: *AAPG Bulletin*, **88**, 1523-1544.

15  
16  
17  
18  
19  
20  
21  
22  
23  
24  
25  
26  
27  
28  
29  
30  
31  
32  
33  
34  
35  
36  
37  
38  
39  
40  
41  
42  
43  
44  
45  
46  
47  
48  
49  
50  
51  
52  
53  
54  
55  
56  
57  
58  
59  
60  
Garcia-Castellanos, D., F. Estrada, I. Jiménez-Munt, C. Gorini, M. Fernández, J. Vergés, and R. De Vicente, 2009. Catastrophic flood of the Mediterranean after the Messinian salinity crisis: *Nature*, **462** (7274), 779-781.

Gaullier, V., 1993, Diapirisme salifère et dynamique sédimentaire dans le bassin Liguro-Provençal : Thèse de 3<sup>ème</sup> cycle, Université de Paris 6, 327pp.

Gaullier, V., J-P. Brun, G. Guérin, H. Lecanu, 1993. Raft tectonics: the effect of residual topography below a salt décollement: *Tectonophysics*, **228**, 363-381.

Gaullier, V., and G. Bellaiche, 1996, Diapirisme liguro-provençal : les effets d'une topographie résiduelle sous le sel messinien. Apports de la modélisation analogique : *Comptes Rendus Académie Sciences, Paris*, **322** (Série IIa), 213-220.

Gaullier, V., B.C. Vendeville, H. Huguen, J. Déverchère, L. Droz, A. Domzig, E. Obone Zue Obame, K. Yelles, and the MARADJA and PROGRES Scientific Parties, 2006, Role of thick-skinned tectonics on thin-skinned salt tectonics in the Western Mediterranean: A comparison between the Algerian and North-Balearic basins: *European Geosciences Union General Assembly, Vienna*, Abstract volume 8, 1029-7006.

## Interpretation

29

1  
2  
3 Gorini, C., A. Le Marrec, and A. Mauffret, 1993, Contribution to the structural and  
4 sedimentary history of the Gulf of Lions (Western Mediterranean), from the ECORS profiles,  
5 industrial seismic profiles and well data: *Bulletin de la Société Géologique de France*, **164**, 353-  
6  
7  
8  
9  
10  
11 363.

12  
13  
14 Gorini, C., L. Montadert, and M. Rabineau, 2015, New imaging of the salinity crisis:  
15  
16 Dual Messinian lowstand megasequences recorded in the deep basin of both the eastern and  
17  
18 western Mediterranean: *Marine and Petroleum Geology*, **66**, 278-294.  
19  
20

21  
22  
23  
24  
25  
26  
27  
28  
29  
30  
31  
32  
33  
34  
35  
36  
37  
38  
39  
40  
41  
42  
43  
44  
45  
46  
47  
48  
49  
50  
51  
52  
53  
54  
55  
56  
57  
58  
59  
60  
Granado, P., R. Urgelés, F. Sàbat, E. Albert-Villanueva, E. Roca, J.A. Muñoz, N.  
Mazzuca, and R. Gambini, in press, Geodynamic framework and hydrocarbon plays of a salt  
giant: The North Western Mediterranean Basin: *Petroleum Geoscience*.

Guennoc, P., J.-P. Réhault, and I. Thinon, 2011, West-Corsica Margin, *in* Seismic atlas of  
the “Messinian Salinity Crisis” markers in the Mediterranean and Black Seas. Lofi et al., 2011.  
Commission for the Geological Map of the World (CGMW): *Mémoires de la Société  
Géologique de France*, **179**, 46-48.

Horsfield, W.T., 1977, An experimental approach to basement controlled faulting:  
*Geologie en Mijnbouw*, **56**, 363-370.

Hudec, M.R. and M.P.A. Jackson, 2004, Regional restoration across the Kwanza Basin,  
Angola: Salt tectonics triggered by repeated uplift of a metastable passive margin: *AAPG  
Bulletin*, **88**, 971-990.

## Interpretation

30

Hudec, M.R. and M.P.A. Jackson, 2011, The salt mine: a digital atlas of salt tectonics: The University of Texas at Austin, Bureau of Economic Geology, Udden Book Series No. 5, AAPG Memoir 99, 305 p.

Hsü, K.J., W.B.F. Ryan, and M.B. Cita, 1973, Late Miocene desiccation of the Mediterranean: *Nature*, **242**, 240-244.

Jolivet, L., C. Gorini, J. Smit, and S. Leroy, 2015, Continental breakup and the dynamics of rifting in back-arc basins: The Gulf of Lion margin: *Tectonics*, **34**, 662-679. doi: [10.1002/2014TC003570](https://doi.org/10.1002/2014TC003570).

Krantz, R.W., 1991, Measurements of friction coefficients and cohesion for faulting and fault reactivation in laboratory models using sand and sand mixtures: *Tectonophysics*, **188**, 203-207.

Lofi, J., C. Gorini, S. Berné, G. Clauzon, T. Dos Reis, W.B.F. Ryan, and M.S. Steckler, 2005, Erosional processes and paleo-environmental changes in the western Gulf of Lions (SW France) during the Messinian Salinity Crisis: *Marine and Petroleum Geology*, **217**, 1-30.

Lofi, J., F. Sage, J. Déverchère, L. Loncke, A. Maillard, V. Gaulier, I. Thinon, H. Gillet, P. Guennoc, and C. Gorini, 2011a, Refining our knowledge of the Messinian Salinity Crisis records in the offshore domain through multi-site seismic arrays: *Bulletin de la Société Géologique de France*, **182**, 163-180.

Lofi, J., J. Déverchère, V. Gaulier, H. Gillet, C. Gorini, P. Guennoc, L. Loncke, A. Maillard, F. Sage, and I. Thinon, 2011b, Seismic atlas of the “Messinian Salinity Crisis” markers

## Interpretation

1  
2  
3 in the Mediterranean and Black Seas. Commission for the Geological Map of the World  
4  
5 (CGMW) : Mémoires de la Société Géologique de France, **179**, 72pp. 1CD.  
6  
7

8  
9 Lohrmann, J., N. Kukowski, J. Adam, and O. Oncken, 2003, The impact of analogue  
10 material properties on the geometry, kinematics, and dynamics of convergent sand wedges:  
11  
12 Journal of Structural Geology, **25**, 1691-1771.  
13  
14  
15

16  
17 Loncke, L., V. Gaullier, J. Mascle, B.C. Vendeville, and L. Camera, 2006, The Nile  
18 deep-sea fan: an example of interacting sedimentation, salt tectonics and inherited subsalt  
19 paleotopographic features: Marine and Petroleum Geology, **23**, 297-315.  
20  
21  
22  
23

24  
25 Loncke, L., B.C. Vendeville, V. Gaullier, and J. Mascle, 2010, Respective contributions  
26 of tectonic and gravity-driven processes on the structural pattern in the Eastern Nile deep-sea  
27 fan : insights from physical experiments: Basin Research, **22**, 765-782.  
28  
29  
30  
31

32  
33 Maillard, A., and A. Mauffret, 1993, Structure et volcanisme dans la fosse de Valence  
34 (Méditerranée Nord-occidentale) : Bulletin de la Société Géologique de France, **164**, 338-365.  
35  
36  
37  
38

39  
40 Maillard, A., V. Gaullier, B.C. Vendeville and F. Odonne, 2003, Influence of differential  
41 compaction above basement steps on salt tectonics in the Ligurian-Provençal Basin, northwest  
42 Mediterranean: Marine and Petroleum Geology, **20**, 13-27.  
43  
44  
45  
46

47  
48 Maldonado, A., H. Got, A. Monaco, S. O'Connell, and L. Mirabile, 1985, Valencia Fan  
49 (northwestern Mediterranean): Distal deposition fan variant: Marine Geology, **62**, 295-319.  
50  
51  
52  
53  
54  
55  
56  
57  
58  
59  
60

## Interpretation

32

1  
2  
3  
4  
5  
6  
7  
8  
9  
Martí, J., J. Mitjavila, E. Roca, and A. Aparicio, 1992, Cenozoic magmatism of the  
Valencia Through (Western Mediterranean): relationship between structural evolution and  
volcanism: *Tectonophysics*, **203**, 145-165.

10  
11  
12  
13  
14  
15  
16  
17  
18  
19  
Marton, L.G., G.C. Tari, and C.T. Lehmann, 2000, Evolution of the Angolan passive  
margin, West Africa, with emphasis on post-salt structural styles, *in* W. Mohriak, and M.  
Talwani, eds., *Atlantic rifts and continental margins*: American Geophysical Union, Geophysical  
Monograph, 115, 129-149.

20  
21  
22  
23  
24  
25  
26  
27  
28  
29  
30  
31  
32  
33  
34  
35  
36  
37  
38  
39  
40  
41  
42  
43  
44  
45  
46  
47  
48  
49  
50  
51  
52  
53  
54  
55  
56  
57  
58  
59  
60  
Mauduit, T., G. Guerin, J-P. Brun, and H. Lecanu, 1997, Raft tectonics : the effects of  
basal slope angle and sedimentation rate on progressive extension: *Journal of Structural  
Geology*, **19** (9), 1219-1239.

Mauduit, T., and J.-P. Brun, 1998, Growth fault/rollover systems: birth, growth, and  
decay: *Journal of Geophysical Research*, **103**, 119-136.

Nelly, G., 1994, *Evaporite sequences in petroleum exploration. 2. Geophysical Methods.*  
GRECO52, CNR French Oil and Gas Industry Association, Technical Committee. Edition  
Technip, Paris, 252 pp.

Obone Zue Obame, E., V. Gaullier, F. Sage, A., Maillard, J. Lofi, B.C. Vendeville, I.  
Thinon, J-P. Réhault and the MAURESC Shipboard Scientific Party, 2011, The sedimentary  
markers of the Messinian Salinity Crisis and their relation with salt tectonics on the Provençal  
margin (Western Mediterranean): Results from the “MAURESC” cruise. Special Issue  
“Miocene-Pliocene geodynamics and paleogeography in the Mediterranean region: eustasy-  
tectonics interference”: *Bulletin de la Société Géologique de France*, **182** (2), 181-196.

## Interpretation

33

1  
2  
3 Peel, F.J., 2014, The engines of gravity-driven movement on passive margins:  
4 Quantifying the relative contribution of spreading vs. gravity sliding mechanisms:  
5  
6 Tectonophysics, **633**, 126-142.  
7  
8

9  
10 Quirk, D.G., N. Schodt, B. Lassen, S.J. Ings, D. Hsu, K.K. Hirsch, and C. Von Nicolai,  
11  
12 2012, Salt tectonics on passive margins: examples from Santos, Campos and Kwanza basins, , *in*  
13 G.I. Alsop, S.G. Archer, A.J. Hartley, N.T. Grant, and R. Hodgkinson, eds., Salt Tectonics,  
14  
15 Sediments and Prospectivity: Geological Society, London Special Publications, 363, 207-244.  
16  
17

18  
19 Roca, E., 2001, The Northwestern Mediterranean Basin (Valencia Trough, Gulf of Lions  
20 and Liguro-Provençal basins): structure and geodynamic evolution, *in* P.A. Ziegler, W. Cavazza,  
21  
22 A.H.F., Robertson, and S. Crasquin-Soleau, eds., Peri-Tethyan Rift/Wrench Basins and Passive  
23  
24 Margins 186, 671-706. Peri-Tethys Memoir, 6: Mémoires du Museum National d'Histoire  
25  
26 Naturelle, Paris.  
27  
28

29  
30 Roca, E., M. Sans, and L. Cabrera, 1999, Modelo tectonosedimentario del sector central  
31  
32 septentrional del Margen Catalán sumergido (cubetas de Barcelona, Sant Feliu, Begur y  
33  
34 Riumors-Rosas), *in* Libro Homenaje a José Ramírez del Pozo. AGGEP, Madrid, 199-217.  
35  
36

37  
38 Roveri, M., M.A. Bassetti, and F. Ricci Lucchi, 2001, The Mediterranean Messinian  
39  
40 salinity crisis: an Apennine foredeep perspective: Sedimentary Geology, **140**, 201-214.  
41  
42

43  
44 Roveri, M., S. Lugli, V. Manzi, and B.C. Schreiber, 2008, The Messinian Sicilian  
45  
46 stratigraphy revisited: new insights for the Messinian salinity crisis: Terra Nova, **20**, 483-488.  
47

48  
49 Rowan, M.G., F.J. Peel, and B.C. Vendeville, 2004, Gravity-driven foldbelts on passive  
50  
51 margins, *in* K.R. McClay, ed., Thrust Tectonics and Hydrocarbon Systems:. AAPG Memoir, 82,  
52  
53 157-182.  
54  
55  
56  
57  
58  
59  
60

Interpretation

34

Rowan, M.G., F.J. Peel, B.C. Vendeville, and V. Gaullier, 2012, Salt tectonics at passive margins: geology versus models – Discussion: *Marine and Petroleum Geology*, **37**, 184-194.

Sans, M., and F. Sàbat, 1993, Oligocene salt rollers and syn-kinematic sediments in the northeast sector of the Valencia trough (western Mediterranean): *Bulletin de la Societé Géologique de France*, **164**, 189-198.

Schettino, A. and E. Turco, 2010, Tectonic history of the western Tethys since the Late Triassic: *GSA Bulletin*, **123**, 89-105.

Stampfli, G.M. and C.F.W. Höcker, 1989, Messinian paleorelief from 3-D seismic survey in the Tarraco concession area (Spanish Mediterranean Sea): *Geology in Mijnbouw*, **68**, 201-210.

Vendeville, B.C. and M.P.A. Jackson, 1992, The rise of diapirs during thin-skinned extension: *Marine and Petroleum Geology*, **9**, 331-353.

#### LIST OF FIGURES

**Figure 1.** Idealized sketch of a salt-bearing passive margin with a basinward-dipping salt detachment (purple polygon) (modified from Rowan *et al.*, 2004). Gravity gliding and spreading of the salt layer trigger the failure of the cover, which is accommodated by upslope extension (listric faults) and downslope contraction (buckle folds) with a translational domain in between. The factors controlling the tilting of the detachment are the differential loading, the thermal subsidence and the tectonic uplift.

## Interpretation

**Figure 2.** Simplified structural map of the Northwestern Mediterranean Basin and surrounding Mediterranean areas (modified from Roca, 2001). Yellow lines indicate the location of the geoseismic sections shown in Figures 3 and 4.

**Figure 3.** Line-drawing across the central part of the northwestern margin of the Liguro-Provençal Basin (southeast of the Gulf of Lions) showing the structure and the sedimentary architecture of the basin infill (modified from Lofi *et al.*, 2011b after Bache *et al.*, 2009). See location in Figure 2.

**Figure 4.** Geoseismic sections across the toe of the northwestern part of the Liguro-Provençal Basin highlighting the gravitational failure structure around three pre-Messinian seamounts (vertical scale in TWTT, see location in Figure 2). They clearly illustrate how the structure of supra-salt units changes depending on the height and the slope of the flanks of pre-salt seamounts. a) Geoseismic section across a seamount with the summit located below the top of the Messinian salt that consequently did not affect the gravitational failure of the margin; b) Geoseismic section across a seamount with the summit located slightly above the top of the Messinian salt, and c) Geoseismic section across a much taller seamount with the summit that crops out on the seafloor. Note that the geometry of the reflectors in figures 4a, 4b and 4c is congruent with that of the structures depicted in our analogue models 3 (Fig. 8b) and 6 (Fig. 13b) respectively.

**Figure 5.** Experimental setup with the terminology used in the description of the models. a) Top-view sketch of the experimental setup with the location of the seamount and the different upslope pinch-out and downslope edge of the analogue evaporitic units; b) Longitudinal cross-section sketch of the setup before deformation (the height of the plasticine seamount “h” changes in our

1 Interpretation

36

2  
3 experimental programme; see Table 1); and c) Experimental stratigraphy with the strength curve  
4 and equivalence with the sedimentary ifill in the deep Liguro-Provençal Basin.  
5  
6  
7

8  
9 **Figure 6.** Comparison between the main structural elements developed by gravitational gliding  
10 at the end of the deformation in a cross-section of the experiment without a seamount  
11 (experiment 0, Table 1) (a); in a cross-section of the experiment 1a cutting a seamount with the  
12 summit located inside the pure polymer layer (b); and (c) in a cross-section of experiment 4  
13 (Table 1) that cuts a seamount with the summit located above the top of the pure polymer layer.  
14  
15

16 LU: Mixed pink polymer and sand (50% by volume) representing the Messinian Lower Unit;  
17 MU: pure transparent polymer that simulates de Messinian Mobile Unit.  
18  
19

20  
21 **Figure 7.** Detailed cross-sections showing the main structures developed around the seamount  
22 during gravitational gliding when the summit is initially located inside the pure polymer layer. a)  
23 Cross-section of experiment 1 (Table 1) after 6 hours of gravitational gliding, b) cross-section of  
24 experiment 1a (Table 1) after 18 hours of gravitational gliding. Note that the pure polymer layer  
25 shows thickness variations, whereas the pink layer (mixture of sand and polymer) does not show  
26 any deformation.  
27  
28  
29  
30  
31  
32  
33  
34  
35  
36  
37  
38  
39  
40  
41

42 **Figure 8.** Detailed cross-sections showing the main structures developed around the seamount  
43 during gravitational gliding before (a) and after (b and c) polymer overthrusting. a) Cross-section  
44 of experiment 4 after 6 hours of gravitational gliding, b) Cross-section of experiment 3 after 18  
45 hours of gravitational gliding, and c) Cross-section of experiment 7 after 34 hours of  
46 gravitational gliding. Note that in Figures 7b and 7c, the pink layer (mixture of sand and  
47 polymer) appears deformed downslope of the seamount, where it is thinner beneath the welded  
48 areas and thicker in the adjacent inflated areas.  
49  
50  
51  
52  
53  
54  
55  
56  
57  
58  
59  
60

## Interpretation

1  
2  
3 **Figure 9.** a to h) Top view pictures draped over the colored relief surfaces created from the  
4 corresponding topography point cloud from the beginning ( $t_0$ ) to the end ( $t_{16}$ ) of experiment 3; i)  
5 Evolution of the topography along the cross-section a-a' during experiment 3 between  $t_0$  to  $t_{16}$ .  
6 The figures show two evolutionary stages: the first one between  $t_0$  and  $t_4$ , characterized by the  
7 progressive rising of the polymer and overlying cover above the upslope flank of the seamount  
8 and the presence of two extensional-contractional pairs separated by the seamount; and the  
9 second one between  $t_6$  and  $t_{16}$  in which the previously rising polymer overthrusts the seamount  
10 and begins to slide down on the downslope seamount flank forming a gravitationally linked fold  
11 and thrust system. During this second stage the two extensional-contractional pairs are  
12 reconnected.  
13  
14  
15  
16  
17  
18  
19  
20  
21  
22  
23  
24  
25  
26  
27

28 **Figure 10.** Slices of experiment 3 made from a 3D voxel that used the final serial sections as a  
29 seed to interpolate sections in every direction (see Dooley *et al.*, 2009). a and b) Inlines that  
30 correspond to real end sections; c) Interpolated depth slice; and d, e, f and g) Interpolated  
31 crosslines. The location of each section is shown in different colors in each image (inlines in  
32 blue; crosslines in purple; and depth slice in yellow). Blue, red and green colors inside the pure  
33 polymer correspond to the deformed polymer color plugs.  
34  
35  
36  
37  
38  
39  
40  
41  
42  
43

44 **Figure 11.** Detail of a cross-section of experiment 3 showing the structure of the downslope  
45 flank of the seamount after 18 hours of gravitational gliding and its correlation with the proposed  
46 evolutionary stages. The development of debrites is highlighted during the progressive rising of  
47 the polymer at the upslope flank of the seamount and during the overthrusting coeval with the  
48 development of the erosive unconformity. Debrite deposits decrease progressively through time,  
49 disappearing with the deposition of layer 6.  
50  
51  
52  
53  
54  
55  
56  
57  
58  
59  
60

1 Interpretation

38

2  
3 **Figure 12.** Top-view photograph (a) and longitudinal cross-section (b) showing the main  
4 structural elements related to the highest seamount (experiment 6, Table 1). The overhead  
5 photograph was taken after 4 hours of gravitational gliding and prior to the deposition of the  
6 upper red layer in Fig. 12b.  
7  
8  
9  
10  
11

12  
13  
14 **Figure 13.** a) Contour map of the top of the pure polymer at the end of experiment 3. The  
15 reference datum of this map (0 value) is the top of the last syn-kinematic sand layer (see Fig. 8b).  
16  
17 b) The top view of the pure polymer layer in model 3 at the end of the experiment shows the  
18 effect of the seamount on the pure polymer flow and on the deformation of the colored polymer  
19 plugs. Welds, diapirs and the final shape of the polymer plugs were reconstructed by digitizing  
20 their position and edges on different depth slices (i.e., in the depth slice represented in Figure  
21 10c). c) Interpreted cross-section through the seamount showing the shape of two polymer plugs  
22 (purple and yellow) at the end of model 3.  
23  
24  
25  
26  
27  
28  
29  
30  
31  
32  
33

34 **Table 1.** Main experimental parameters for the physical models described in this article. \* The  
35 slope angle corresponds to the value of the average angle of the seamount flanks.  
36  
37  
38  
39

40 **Table 2.** Scaling parameters used in the experimental program presented in this study.  
41  
42  
43  
44  
45  
46  
47  
48  
49  
50  
51  
52  
53  
54  
55  
56  
57  
58  
59  
60

**Table 1.** Experimental program

Experiment	Seamount height (mm)	Slope angle*	Time (hours)
Exp_0	no seamount	-	6
Exp_1	21	23°	6
Exp_1a	21	23°	18
Exp_2	28	29°	18
Exp_3	35	35°	18
Exp_4	35	35°	6
Exp_5	45	42°	6
Exp_6	55	48°	6
Exp_7	35	35°	34

\* Average slope angle of seamount flanks

For Peer Review

**Table 2.** Scaling parameters used in the experimental program

Quantity	Experiment	Nature	Ratio
<b>Thickness</b>			
<i>Overburden</i>	5-30 mm	300 m - 2 km	$1.6 \times 10^{-5}$ - $1.5 \times 10^{-5}$
<i>Upper Messinian Unit</i>	6 mm	500 - 600 m	$1.09 \times 10^{-5}$
<i>Mobile Messinian Unit</i>	10 mm	0 - 3 km	$1.8 \times 10^{-5}$
<i>Lower Messinian Unit</i>	5 mm	400 - 500 m	$1.1 \times 10^{-5}$
<b>Density</b>			
<i>Overburden</i>	1500 kg m <sup>-3</sup>	2.300 kg m <sup>-3</sup>	0.65
<i>Upper Messinian Unit</i>	1500 kg m <sup>-3</sup>	2.600 kg m <sup>-3</sup>	0.57
<i>Mobile Messinian Unit</i>	972 kg m <sup>-3</sup>	2.200 kg m <sup>-3</sup>	0.46
<i>Lower Messinian Unit</i>	1550 kg m <sup>-3</sup>	2.600 kg m <sup>-3</sup>	0.59
<b>Density contrast</b>			
<i>UU / MU</i>	528	500	1.05
<i>MU / LU</i>	578	500	1.56
<b>Ductile layer viscosity</b>			
<i>Mobile Messinian Unit</i>	$1.6 \times 10^{-4}$ Pa s *	$10^{-18}$ - $10^{-19}$ Pa s	$1.6 \times 10^{-14}$ - $1.6 \times 10^{-15}$ Pa s
<i>Lower Messinian Unit</i>	$3.34 \times 10^{-4}$ Pa s *	unkown	--
<b>Overburden coefficient of internal friction</b>			
	0.69	0.8	0.86
<b>Gravity acceleration</b>			
	9.81 m.s <sup>-2</sup>	9.81 m.s <sup>-2</sup>	1

\* Viscosity measured when deformed at a laboratory strain rate of  $1.83 \times 10^{-4}$  cm s<sup>-1</sup>

1  
2  
3  
4  
5  
6  
7  
8  
9  
10  
11  
12  
13  
14  
15  
16  
17  
18  
19  
20  
21  
22  
23  
24  
25  
26  
27  
28  
29  
30  
31  
32  
33  
34  
35  
36  
37  
38  
39  
40  
41  
42  
43  
44  
45  
46  
47  
48  
49  
50  
51  
52  
53  
54  
55  
56  
57  
58  
59  
60

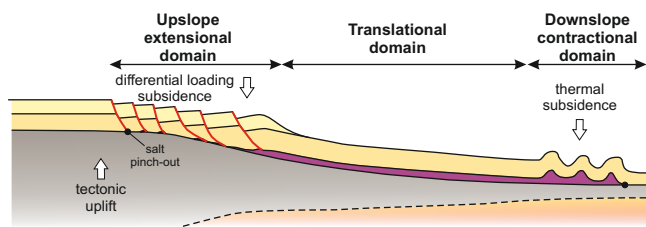


Figure 1

For Peer Review

1  
2  
3  
4  
5  
6  
7  
8  
9  
10  
11  
12  
13  
14  
15  
16  
17  
18  
19  
20  
21  
22  
23  
24  
25  
26  
27  
28  
29  
30  
31  
32  
33  
34  
35  
36  
37  
38  
39  
40  
41  
42  
43  
44  
45  
46  
47  
48  
49  
50  
51  
52  
53  
54  
55  
56  
57  
58  
59  
60

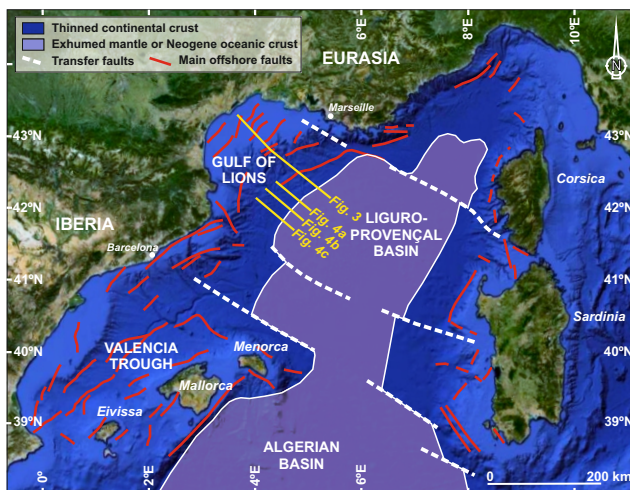


Figure 2

For Peer Review

1  
2  
3  
4  
5  
6  
7  
8  
9  
10  
11  
12  
13  
14  
15  
16  
17  
18  
19  
20  
21  
22  
23  
24  
25  
26  
27  
28  
29  
30  
31  
32  
33  
34  
35  
36  
37  
38  
39  
40  
41  
42  
43  
44  
45  
46  
47  
48  
49  
50  
51  
52  
53  
54  
55  
56  
57  
58  
59  
60

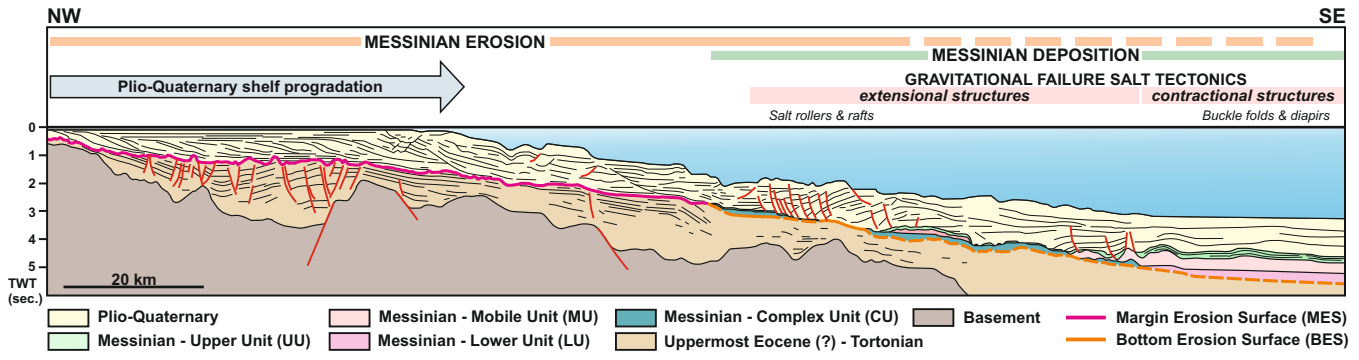


Figure 3

For Peer Review

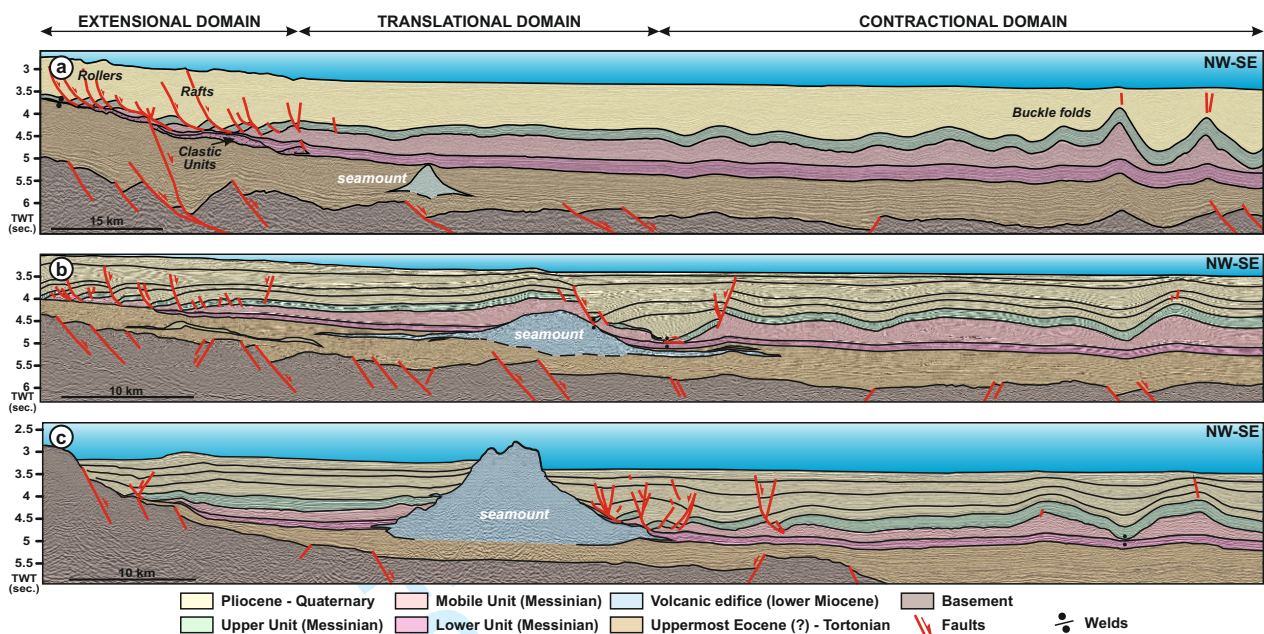
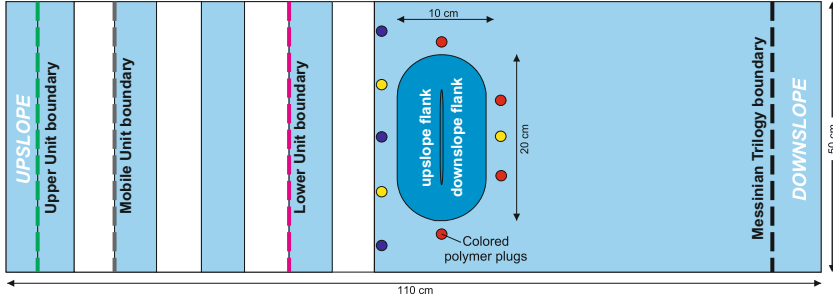


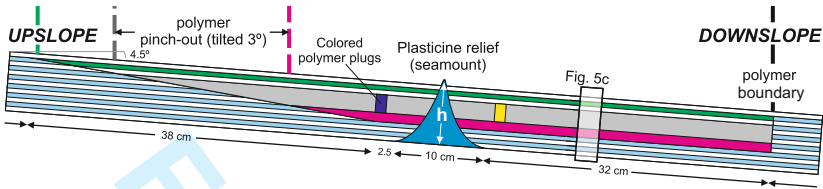
Figure 4

1  
2  
3  
4  
5  
6  
7  
8  
9  
10  
11  
12  
13  
14  
15  
16  
17  
18  
19  
20  
21  
22  
23  
24  
25  
26  
27  
28  
29  
30  
31  
32  
33  
34  
35  
36  
37  
38  
39  
40  
41  
42  
43  
44  
45  
46  
47  
48  
49  
50  
51  
52  
53  
54  
55  
56  
57  
58  
59  
60

a) Experimental setup plan view without Messinian analogues



b) Experimental setup section view



c) Seismic and experimental stratigraphy

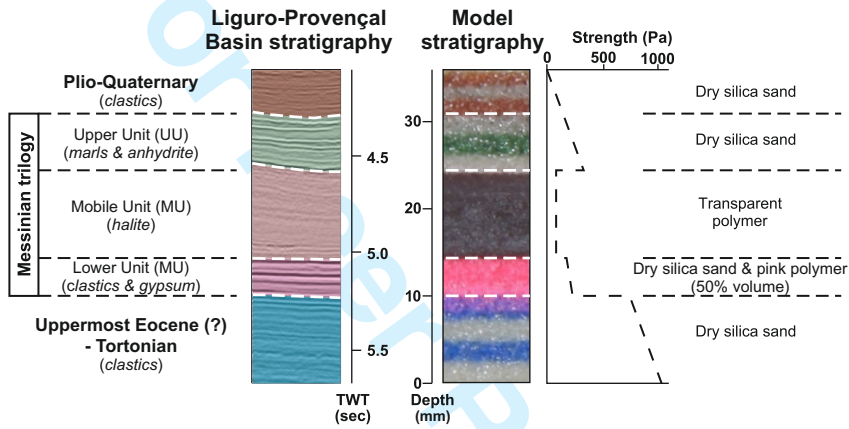
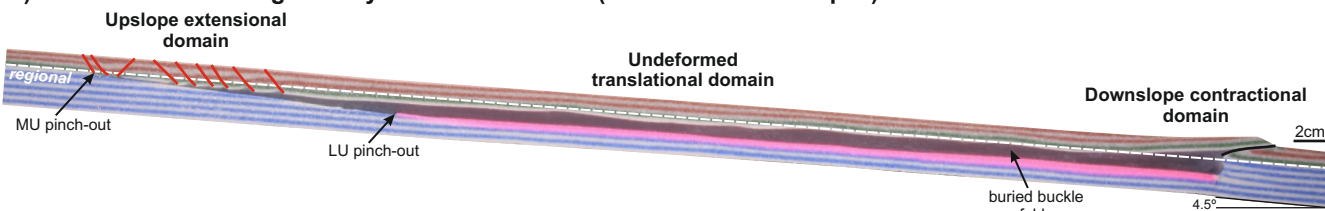
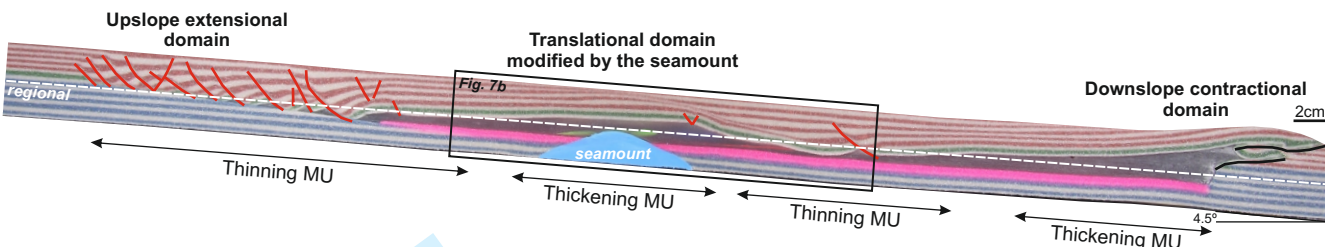


Figure 5

a) Gravitational failure geometry without seamount (baseline model - Exp. 0)



b) Gravitational failure geometry with seamount summit inside the pure polymer layer (Exp. 1a)



c) Gravitational failure geometry with seamount summit above the pure polymer layer (Exp. 4)

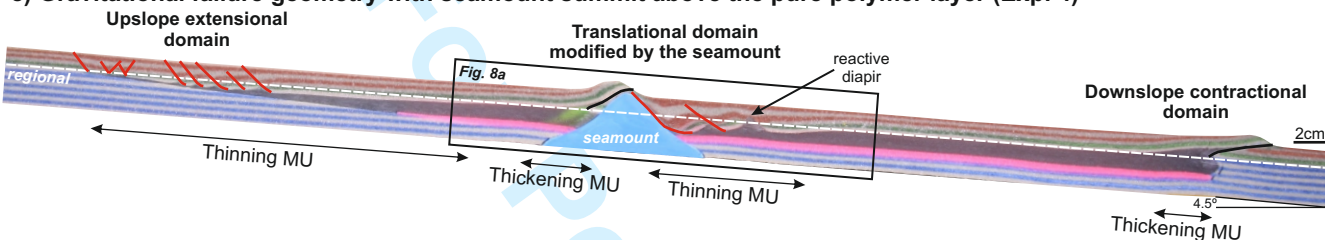


Figure 6

1  
2  
3  
4  
5  
6  
7  
8  
9  
10  
11  
12  
13  
14  
15  
16  
17  
18  
19  
20  
21  
22  
23  
24  
25  
26  
27  
28  
29  
30  
31  
32  
33  
34  
35  
36  
37  
38  
39  
40  
41  
42  
43  
44  
45  
46  
47  
48  
49  
50  
51  
52  
53  
54  
55  
56  
57  
58  
59  
60

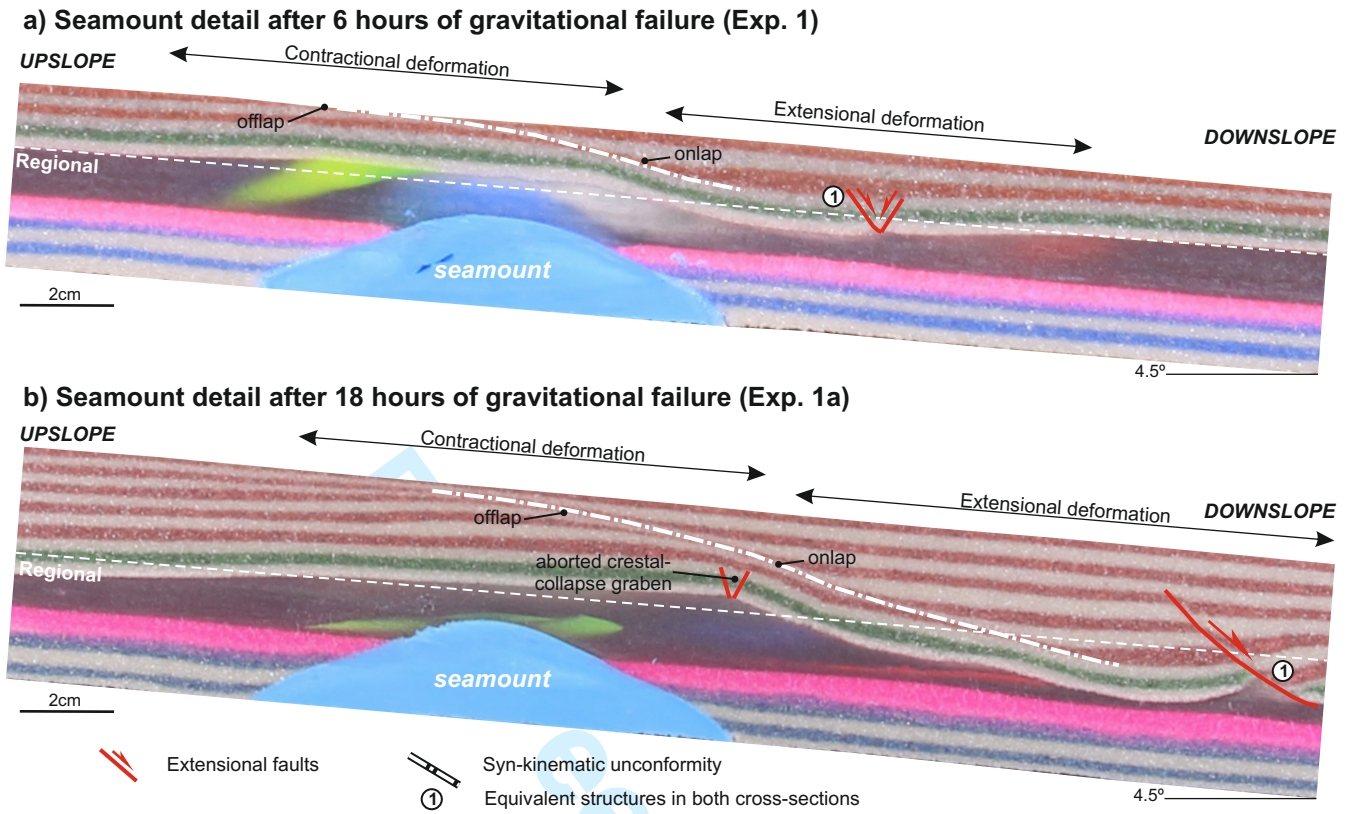
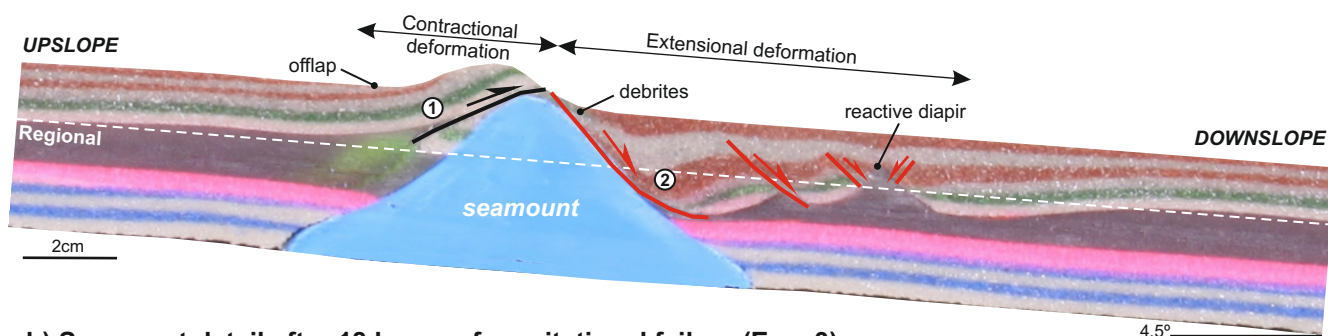


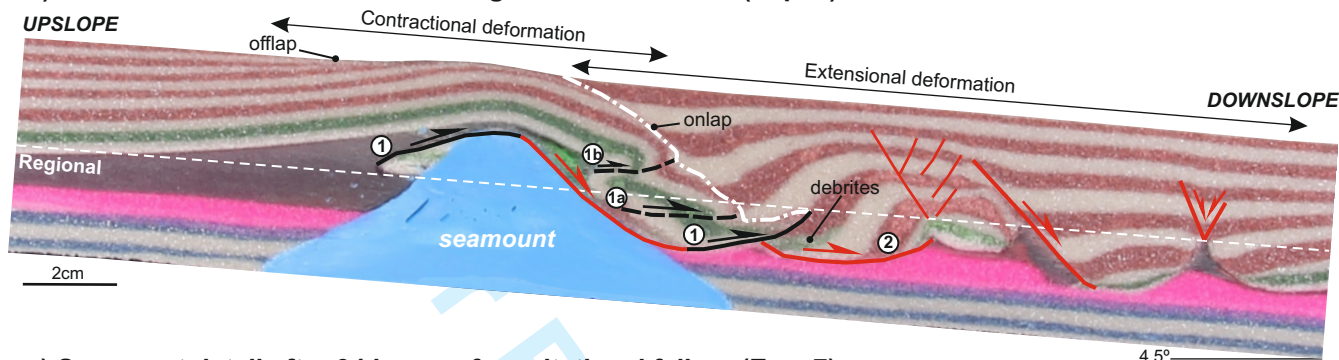
Figure 7

1  
2  
3  
4  
5  
6  
7  
8  
9  
10  
11  
12  
13  
14  
15  
16  
17  
18  
19  
20  
21  
22  
23  
24  
25  
26  
27  
28  
29  
30  
31  
32  
33  
34  
35  
36  
37  
38  
39  
40  
41  
42  
43  
44  
45  
46  
47  
48  
49  
50  
51  
52  
53  
54  
55  
56  
57  
58  
59  
60

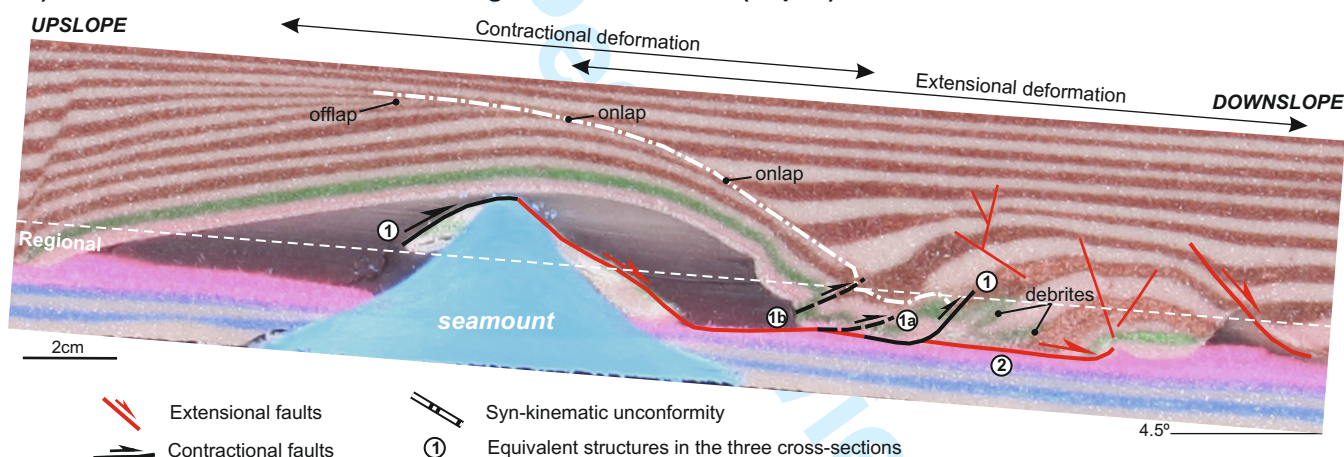
a) Seamount detail after 6 hours of gravitational failure (Exp. 4)



b) Seamount detail after 18 hours of gravitational failure (Exp. 3)



c) Seamount detail after 34 hours of gravitational failure (Exp. 7)



- Extensional faults
- Contractional faults
- Syn-kinematic unconformity
- Equivalent structures in the three cross-sections

Figure 8

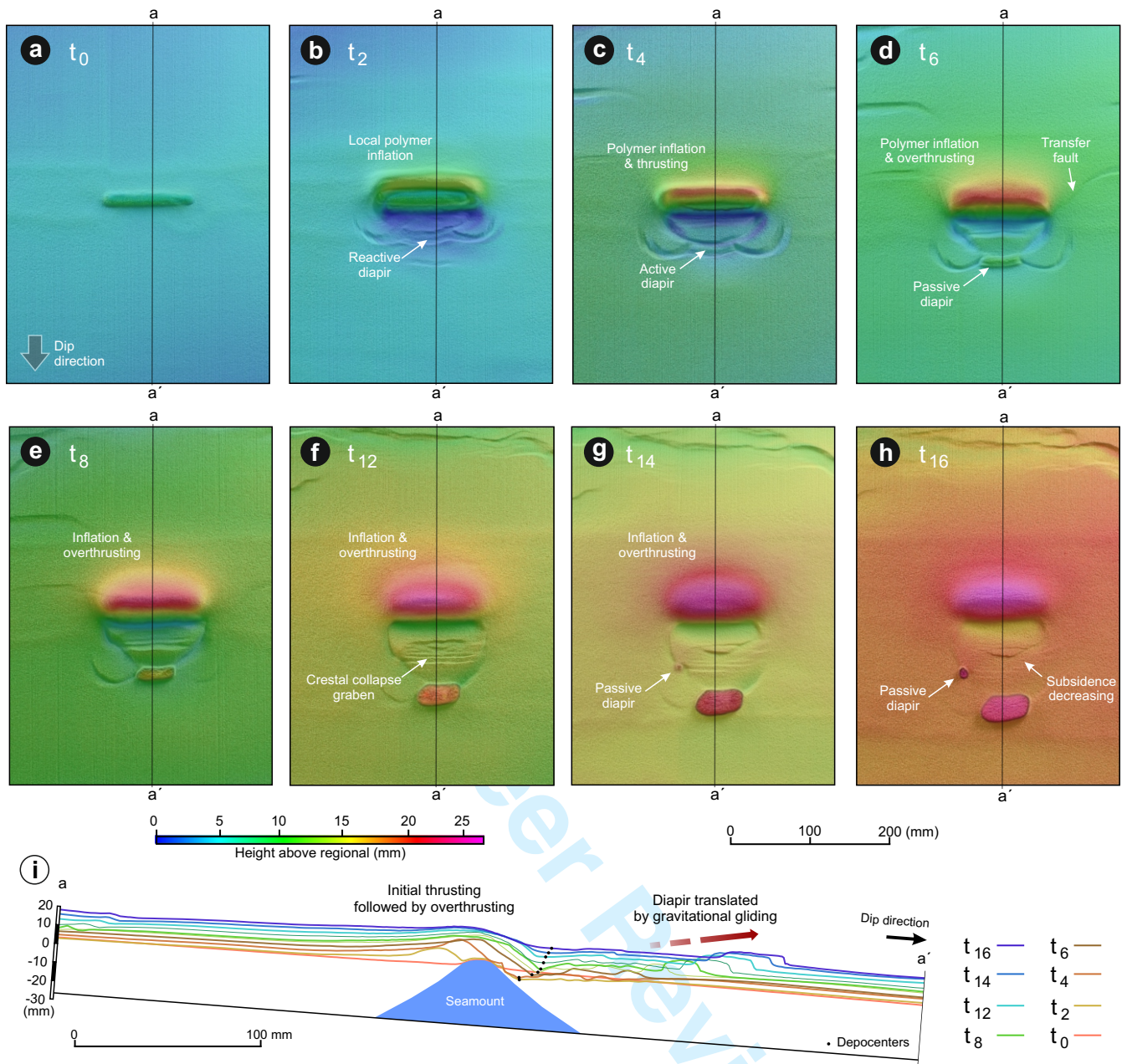
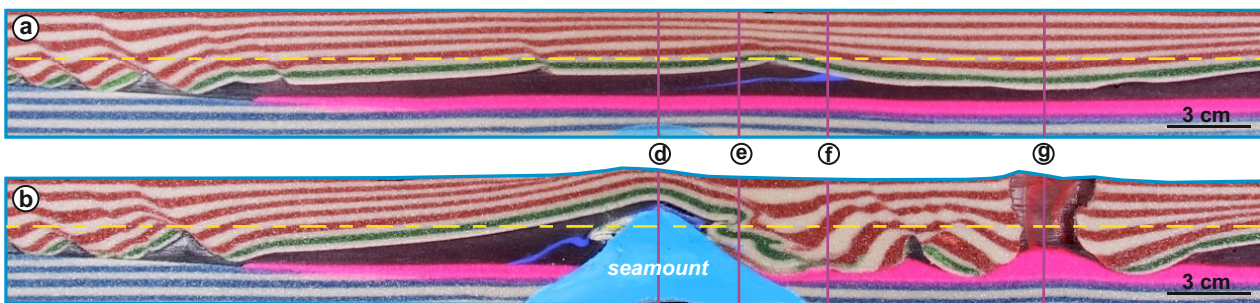
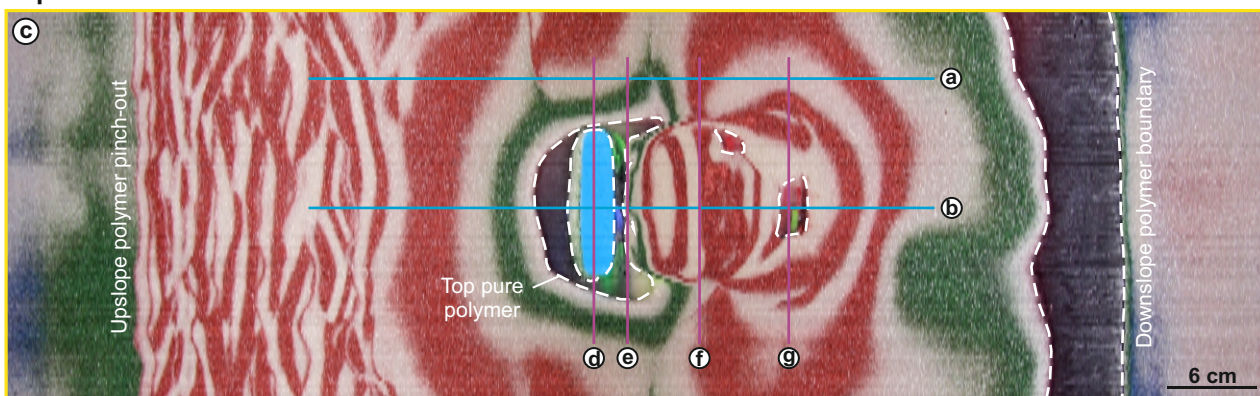


Figure 9

Inlines



Depth slice



Crosslines

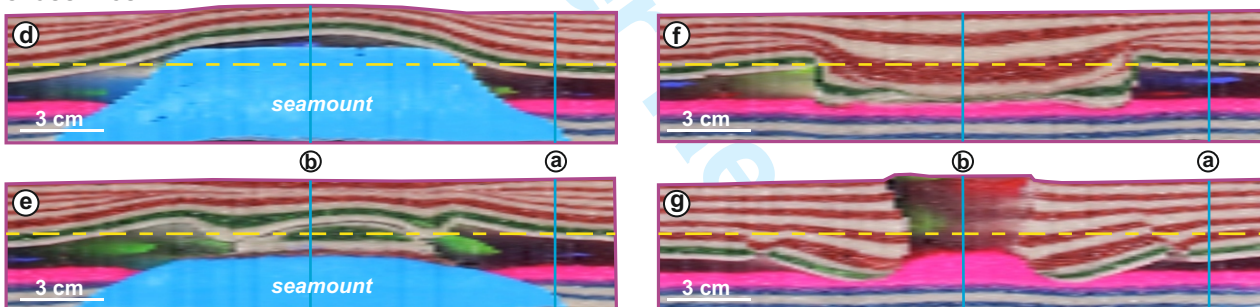


Figure 10

1  
2  
3  
4  
5  
6  
7  
8  
9  
10  
11  
12  
13  
14  
15  
16  
17  
18  
19  
20  
21  
22  
23  
24  
25  
26  
27  
28  
29  
30  
31  
32  
33  
34  
35  
36  
37  
38  
39  
40  
41  
42  
43  
44  
45  
46  
47  
48  
49  
50  
51  
52  
53  
54  
55  
56  
57  
58  
59  
60

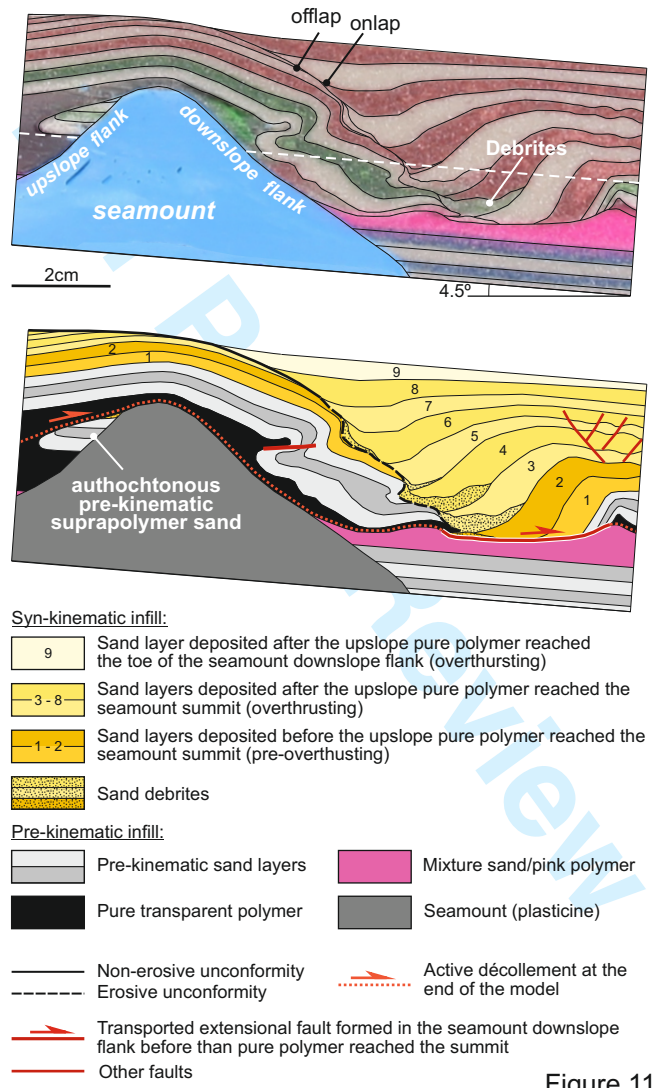


Figure 11

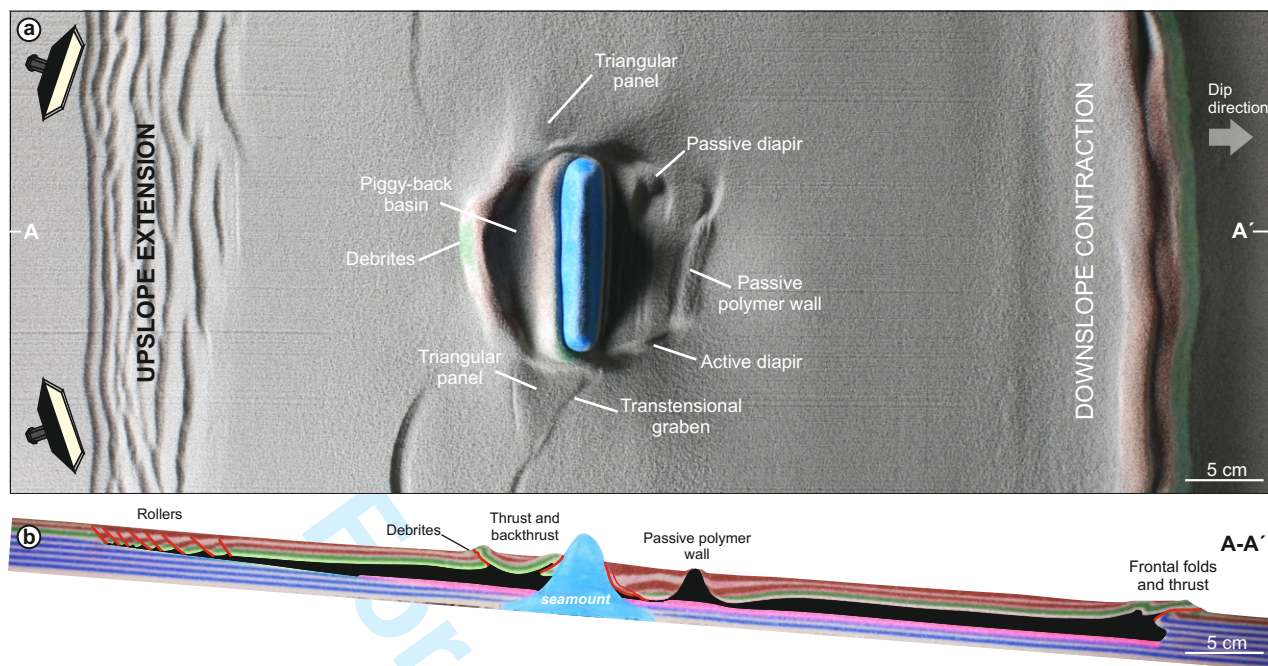


Figure 12

1  
2  
3  
4  
5  
6  
7  
8  
9  
10  
11  
12  
13  
14  
15  
16  
17  
18  
19  
20  
21  
22  
23  
24  
25  
26  
27  
28  
29  
30  
31  
32  
33  
34  
35  
36  
37  
38  
39  
40  
41  
42  
43  
44  
45  
46  
47  
48  
49  
50  
51  
52  
53  
54  
55  
56  
57  
58  
59  
60

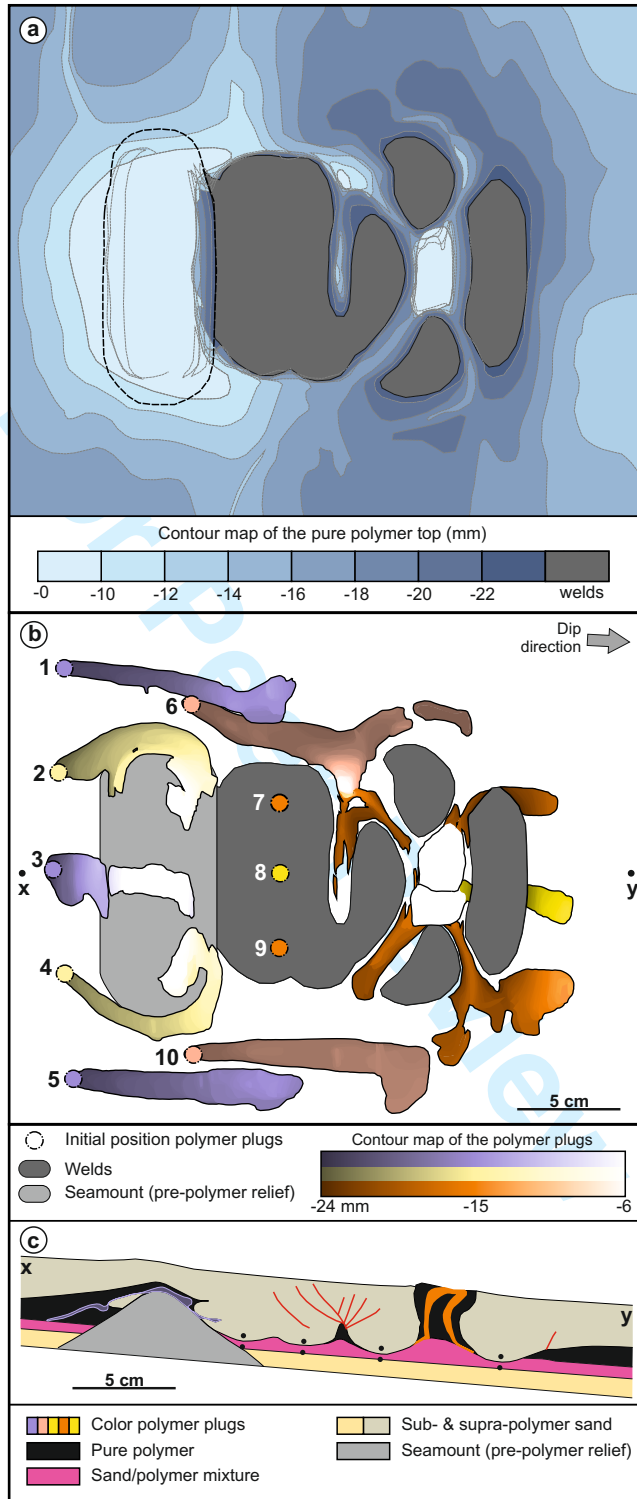


Figure 13